

Unravelling somatosensory connectivity with peripheral and central stimulation

Oskari Ahola

School of Science

Thesis submitted for examination for the degree of Master of
Science in Technology.

Espoo 22.12.2022

Supervisor

Prof. Lauri Parkkonen

Advisor

D.Sc. (Tech.) Tuomas Mutanen



Aalto University
School of Science

Copyright © 2022 Oskari Ahola

Author Oskari Ahola		
Title Unravelling somatosensory connectivity with peripheral and central stimulation		
Degree programme Life Science Technologies		
Major Human Neuroscience and Technology		Code of major SCI3061
Supervisor Prof. Lauri Parkkonen		
Advisor D.Sc. (Tech.) Tuomas Mutanen		
Date 22.12.2022	Number of pages 52+6	Language English

Abstract

Sensations corresponding to somatosensory stimuli, such as touch, pain and temperature are a part of our everyday lives. In the cortex, the primary and secondary somatosensory cortices (SI and SII, respectively) are responsible for processing somatosensory information. Magneto- and electroencephalography (MEG and EEG, respectively) with simultaneous peripheral nerve stimulation have been used successfully in measuring activation patterns of SI and SII, which have been shown to activate at different latencies. However, the nature of connectivity between SI and SII has not been unravelled. With transcranial magnetic stimulation (TMS), SI can be stimulated without activating the natural extracephalous somatosensory pathways. Different activation patterns evoked by peripheral and central stimulation provide essential information for assessing the nature of connectivity between SI and SII.

In this Master's thesis, the spatiotemporal activation patterns of SI and SII evoked by electric median nerve stimulation (MNS) at the left wrist were examined from seven subjects with simultaneous MEG and EEG measurements. The individual location of initial SI activation based on MEG was used in stimulation targeting in TMS. Based on individual anatomical magnetic resonance images and the multimodal MEG–EEG data, individually-calibrated head models were constructed to enhance the EEG forward models used in analyzing TMS–EEG data. TMS–EEG source modelling was done using spatial priors based on the locations of initial SI and SII activation found from MEG data. For both stimulation modalities, the source time courses were estimated and used to analyze the activation dynamics between SI and SII.

Both stimulation modalities were found to evoke activation in the right SI and bilaterally in SII. The different bilateral activation patterns of SII across hemispheres and stimulation modalities suggest that SII receives information both from the peripheral nervous system via thalamocortical pathways and from SI. The earlier and stronger peaks of the right-hemisphere SII due to electric MNS at the left wrist suggest that the contralateral SII activates first, and is dominant in processing unilateral somatosensory stimuli.

Keywords primary somatosensory cortex, secondary somatosensory cortex, somatosensory connectivity, magnetoencephalography, electroencephalography, transcranial magnetic stimulation, median nerve stimulation

Tekijä Oskari Ahola

Työn nimi Somatosensoristen alueiden konnektiivisuuksien määrittely perifeerisellä sekä sentraalisella stimulaatiolla

Koulutusohjelma Life Science Technologies

Pääaine Human Neuroscience and Technology**Pääaineen koodi** SCI3061

Työn valvoja Prof. Lauri Parkkonen

Työn ohjaaja TkT Tuomas Mutanen

Päivämäärä 22.12.2022**Sivumäärä** 52+6**Kieli** Englanti

Tiivistelmä

Tuntoaistimuksia tuottavat ärsykkeet, kuten kosketus, kipu ja lämpö ovat osana jokapäiväistä elämäämme. Primaarinen ja sekundaarinen tuntoaivokuori (SI ja SII) ovat pääasiallisesti vastuussa tuntoaistimuksiin liittyvästä prosessoinnista. Somatosensoristen aivokuorten aktivaatioita on onnistuttu mallintamaan käyttäen perifeerisellä stimuluksella herätettyä magneto- ja elektroenkefalografista (MEG ja EEG) dataa, minkä avulla SI- ja SII-alueiden aktivaatioiden on todettu esiintyvän erilaisilla aikaviiveillä. Tosin tällä hetkellä tuntoaivokuorten välisistä mahdollisista kulkuyhteyksien luonteesta ei ole varmaa tietoa. Transkraniaalisella magneettistimulaatiolla (TMS) on mahdollista stimuloida sentraalisesti SI-aivokuorta ohittamalla luonnolliset aivojen ulkopuoliset somatosensoriset reitit. Erilaiset perifeerisellä ja sentraalisella stimulaatiolla herätetyt tuntoaivokuorten vasteet kertovat tuntoaivokuoren alueiden järjestäytyneisyydestä.

Tässä diplomityössä SI- ja SII-aivokuorten MEG- ja EEG-herätevasteita mitattiin seitsemältä koehenkilöltä käyttäen vasemman ranteen sähköistä medianus-hermon stimulaatiota (MNS). MEG-datasta lokalisoituja ensisijaisia SI-vasteita käytettiin myöhemmin samanlaisen TMS-EEG -mittausprotokollan stimulaation kohdentamiseen. Koehenkilöiden yksilöllisiä aivojen magneettikuvia sekä medianus-hermon stimulaation herättämiä SI-alueen MEG-EEG-vasteita käytettiin yksilöllisten päämallien kalibrointiin tarkkaa TMS-EEG-lähdemallinnusta varten. MEG-datasta lokalisoituja ensisijaisten SI- ja SII-vasteiden paikkoja käytettiin spatiaalisina ennakkoina TMS-EEG -herätevasteiden lähdemallinnukseen.

MNS- ja TMS-protokollien herättämien vasteiden aikasarjat estimoitii SI- ja SII-alueilta. Erilaiset stimulusmodaaleilla herätetyt SII-aivokuorten bilateraaliset aktivaatiot viittaavat siihen, että SII saa informaatiota sekä ääreishermostolta talamokortikaalisten yhteyksien välityksellä että SI-aivokuorelta. Aikaisemmat ja vahvemmat vasemman ranteen sähköisen MNS-protokollan herättämät oikean aivopuoliskon SII-aktivaatioiden piikit viittaavat siihen, että kontralateraalinen SII-aivokuori aktivoituu ensin ja on hallitsevassa roolissa unilateraalisten somatosensoristen ärsykkeiden prosessoinnissa.

Avainsanat primaarinen tuntoaivokuori, sekundaarinen tuntoaivokuori, tuntoaivokuorten yhteydet, magnetoenkefalografia, elektroenkefalografia, transkraniaalinen magneettistimulaatio, medianus-hermon stimulaatio

Acknowledgements

Ranging from applying for an ethical permit to multimodal MEG–EEG and consequential TMS–EEG measurements as well as to data analysis, this work has well prepared me further to the world and working life of neuroscience. I am very grateful that I got to work with concepts that were in line with my wishes and interests; to my understanding, the freedom of research given to a Master’s student is typically narrower.

Thank you Lauri Parkkonen, the thesis supervisor, for providing me the chance to work on this interesting multimodal topic, and for your expert-level advice and reassurances with MEG-related tasks. Thank you Tuomas Mutanen, the thesis advisor, for introducing me to the world of TMS–EEG and for your persistence in trialing multiple sophisticated source modelling methods with me. Although we settled on a more simplistic approach, the lessons learnt in constructing multiple different spatial filters did not go to waste. Special thanks to the funder of this thesis work, Bittium Biosignals Oy, and the representatives of the company, Mikko Hallanoro, Jukka Kinnunen, and Simo-Pekka Simonaho, for providing me with a joint research opportunity, and for their ongoing trust and encouragements in my work.

I would also like to thank Mia Illman, Pantelis Lioumis, and Giulia Pieramico, as well as other personnel from Aalto NeuroImaging and TMS-group, for providing measurement equipment and assisting with the measurements. I also want to thank Aalto Brain Centre for funding the measurements.

I would like to acknowledge that figures in this thesis have been created with the MNE-software, Matplotlib, and BioRender.com.

Espoo, 22.12.2022

Oskari A. Ahola

Contents

Abstract	3
Abstract (in Finnish)	4
Acknowledgements	5
Contents	6
Symbols and abbreviations	8
1 Introduction	10
2 Background	11
2.1 Principles of magneto- and electroencephalography	11
2.1.1 Signal basis at the neural level	11
2.1.2 Measured signals	12
2.1.3 Sensitivities and complementary information	14
2.1.4 Current dipoles	15
2.1.5 Inverse problem and minimum-norm estimation	15
2.2 Principles of transcranial magnetic stimulation	16
2.3 Somatosensory system	18
2.3.1 Primary somatosensory cortex	18
2.3.2 Activation patterns of the primary somatosensory cortex	20
2.3.3 Secondary somatosensory cortex	21
2.3.4 Somatosensory lesions	22
3 Methods	23
3.1 Experiment	23
3.1.1 Magneto- and electroencephalography	24
3.1.2 Transcranial magnetic stimulation	25
3.2 Pre-processing	25
3.3 Head modelling	28
3.4 Source modelling	31
3.4.1 Responses evoked by median nerve stimulation	31
3.4.2 Responses evoked by transcranial magnetic stimulation	32
3.5 Latency detection	33
3.6 Global field amplitude	33
3.7 Model validation	34
4 Results	35
4.1 Evoked responses	35
4.2 Skull conductivity	37

4.3 Somatosensory sources	38
5 Discussion	41
6 Conclusion	45
References	46
Appendix	53
A Measurement information	53
B Sensor selection	54
C TEP peak topographies	56
D Somatosensory time courses	58

Symbols and abbreviations

Symbols

\mathbf{B}	Magnetic field
\mathbf{E}	Total electric field
\mathbf{E}_p	Primary electric field
\mathbf{E}_s	Secondary electric field
\mathbf{J}	Total current density
\mathbf{J}_p	Primary current density
\mathbf{J}_v	Volume current density
\mathbf{L}	Forward operator/solution (lead field matrix)
\mathbf{m}	Measured data
\mathbf{s}	Source time course
V	Potential
δ	Dirac delta function
ε_0	Vacuum permittivity
λ	Regularization parameter
μ_0	Vacuum permeability
ρ	Charge density
σ	Conductivity
$\widehat{(\cdot)}$	Estimate of (\cdot)

Operators

$\mathbf{A} \times \mathbf{B}$	Cross product between vectors \mathbf{A} and \mathbf{B}
$\mathbf{A} \cdot \mathbf{B}$	Dot product between vectors \mathbf{A} and \mathbf{B}
$\ \mathbf{s}\ ^2$	L2 norm of \mathbf{s}
\mathbf{D}^T	Transpose of matrix \mathbf{D}
\mathbf{D}^{-1}	Inverse of matrix \mathbf{D}
\mathbf{D}^\dagger	Pseudoinverse of matrix \mathbf{D}
∇	Nabla
$\nabla \times \mathbf{A}$	Curl of vector \mathbf{A}
$\nabla \mathbf{A}$	Gradient of vector \mathbf{A}
∂	Partial derivative
$\int_{\mathcal{C}}$	Integral over \mathcal{C}
\sum_i	Sum over index i

Abbreviations

BA	Brodmann area
BEM	Boundary element method
COBYLA	Constrained Optimization BY Linear Approximation
ECD	Equivalent current dipole
EEG	Electroencephalography
EMG	Electromyography
EOG	Electrooculogram
GFA	Global field amplitude
GoF	Goodness of Fit
HPI	Head position indicator
ICA	Independent component analysis
IAPB	Left abductor pollicis brevis muscle
LSE	Least squares estimation
MEG	Magnetoencephalography
MNE	Minimum-norm estimate
MNS	Median nerve stimulation
MRI	Magnetic resonance imaging
N20(m)	Negative initial response (magnetically measured) of SI due to PNS
nTMS	Navigated transcranial magnetic stimulation
NX(m)	Negative response at X ms (magnetically measured) of SI due to PNS
OP1/4	Cytoarchitectonic areas 1 and 4 in the human parietal operculum
P35(m)	Positive secondary response (magnetically measured) of SI due to PNS
P100(m)	Positive bilateral response (magnetically measured) of SII due to PNS
PNS	Peripheral nerve stimulation
PV	Parietal ventral area
PX(m)	Positive response at X ms (magnetically measured) of SI due to PNS
rMT	Resting motor threshold
S2 _{sub}	Subarea of SII
SI	Primary somatosensory cortex
SII	Secondary somatosensory cortex
SD	Standard deviance
SEF	Somatosensory evoked field
SEM	Standard error of the mean
SEP	Somatosensory evoked potential
SNR	Signal-to-noise ratio
SOUND	Source-estimate-utilizing noise-discarding algorithm
SSP	Signal-space projection
SSP-SIR	Signal-space projection and source-informed reconstruction algorithm
SSS	Signal space separation
SVD	Singular value decomposition
TMS	Transcranial magnetic stimulation
X _T	Evoked response at X ms due to SI TMS

1 Introduction

The somatosensory system is responsible for the processing of somatic sensations including temperature, nociception (sense of pain), proprioception (sense of bodily position), and tactile information. In the cortex, somatosensory stimuli are mainly represented by the activation of the somatosensory cortex composed of the primary and secondary somatosensory cortices (SI and SII, respectively). In the somatosensory cortex, SII acts mostly as a supportive unit for SI – the main and initial processing unit of somatic sensations, and has been shown to play a role in memory and pain-related processing of sensory stimuli [1, 2, 3].

Magneto- and electroencephalography (MEG and EEG, respectively) are non-invasive functional neuroimaging methods respectively measuring neurally induced extracranial magnetic fields and electric potential differences at the scalp, and have been used successfully in measuring somatosensory activation patterns [4, 5]. In response to electric median nerve stimulation (MNS) of the wrist, the initial activation of the contralateral SI appears at a latency of approximately 20 ms (N20 response) [4, 6, 7]. In turn, SII activates bilaterally at latency of approximately 70–90 ms (P100 response) after the activation of SI [4, 6, 8]. However, the nature of connectivity between SI and SII has not been unravelled – while SI receives information via thalamocortical pathways, the thalamo-, corticothalamo-, or corticocortical nature of pathways to SII from the peripheral nervous system or from SI, is still up for debate [8, 9].

Transcranial magnetic stimulation (TMS) is a non-invasive method used to evoke brain activity by targeting rapidly changing magnetic fields to the cortex [10, 11]. With TMS, SI can be stimulated directly without activating the natural extracephalous somatosensory pathways to SI. Hence, using navigated TMS to SI provides essential information on the nature of possible intra- and inter-hemispherical connectivity between SI and SII when comparing their respective signal patterns to the MNS-evoked responses.

The aim of this Master’s thesis is to infer the nature of somatosensory connectivity between SI and SII by comparing responses in those areas evoked by electrical MNS at the left wrist and TMS targeted at the right-hemisphere SI. The hypothesis is that SII receives both signals from the peripheral nervous system via thalamocortical pathways without the intervention of SI and from SI via corticocortical and/or corticothalamocortical pathways, and that there are inter-hemispherical differences in the responsiveness of SII. To assess the hypothesis, the measured SII waveforms and respective peak latencies were analyzed. It is reasonable to assume that if SII is activated bilaterally without inter-hemispherical delays, then SI and SII are not directly engaged. In turn, decreases in the duration of inter-hemispherical SII responses due to TMS over MNS would suggest that SII receives both information from the peripheral nervous system via thalamocortical pathways and information from SI via corticocortical or corticothalamocortical pathways. Furthermore, no TMS-evoked activation at SII would suggest that SII only receives information from the peripheral nervous system via thalamocortical pathways.

2 Background

2.1 Principles of magneto- and electroencephalography

Magneto- and electroencephalography (MEG and EEG) are direct non-invasive functional neuroimaging methods respectively measuring electrical brain activity and the respectively induced magnetic fields. This section presents the physiological and physical basis of MEG and EEG signals as well as the practical and theoretical similarities and differences between the two measurement methods.

2.1.1 Signal basis at the neural level

On a neural level, all of our perceptions and actions are depicted as electrical signals in the nervous system. Travelling along the neuronal conductors of the human body, axons and dendrites, action potentials are able to reach their respective terminating points all around the body, for example, in the brain or in the muscles.

Synapses are gateways permitting inter-neuronal electrical and chemical signal transmission and mostly exist between the end of the axon of a presynaptic neuron and the dendrite or soma of the postsynaptic neuron. Action potentials drive synaptic activity by inducing the release of neurotransmitters to the synaptic cleft. The released neurotransmitters bind to the receptors of the postsynaptic terminal, which regulates the opening and closing of ion channels enabling the in- and outflux of ions, which causes shifts in intra- and extracellular ion concentrations. Consequently, membrane depolarization or hyperpolarization of the postsynaptic neuron is induced respectively depicted as excitatory or inhibitory postsynaptic potentials [12]. Furthermore, the decay of membrane potential differences in the postsynaptic neuron gives rise to the possible initiation of a new action potential.

The brain is a heterogeneous dynamic electrical circuit that has operating points for distinct types of signals that drive our somatic and autonomic responses. In the cortex, pyramidal neurons are the most populous excitatory cell type which are responsible for MEG and EEG -observable responses due to their parallel apical dendrites [13, 14]. Both temporal and spatial summation of neural signal -induced fields are needed for observable responses when using MEG or EEG. Due to the rapid and quadrupolar nature of action potentials, action-potential-induced fields have little to no spatiotemporal summation even in a highly active neuronal cluster. However, the neurotransmitter-driven postsynaptic primary currents $\mathbf{J}_p(\mathbf{r}, t)$ shown in Figure 1a are dipolar and slowly temporally decaying, which enables spatiotemporal summation of the neural signal -induced fields, especially arising from parallelly oriented dendrites of pyramidal neurons in upper cortical layers [14].

Primary currents give rise to accumulating charge densities $\rho(\mathbf{r}, t)$, which induce an electric field (E-field) $\mathbf{E}(\mathbf{r}, t) = -\nabla V(\mathbf{r}, t)$, where V is the electric potential, in the surrounding medium (see Equation 12). The induced E-field $\mathbf{E}(\mathbf{r}, t)$ instigates passive tissue conductivity $\sigma(\mathbf{r})$ -dependent ohmic volume current flow $\mathbf{J}_v(\mathbf{r}, t) = \sigma(\mathbf{r})\mathbf{E}(\mathbf{r}, t)$ in the surrounding medium. Consequently, the electrical components in the brain inducing MEG and EEG signals can

be expressed as the spatial summation [12]

$$\mathbf{J} = \mathbf{J}_p + \mathbf{J}_v, \quad (1)$$

of the primary and volume current densities.

2.1.2 Measured signals

All currents induce a magnetic field, which is the physical basis of MEG signals. By the Biot–Savart law, the total magnetic field \mathbf{B} at a location \mathbf{r} induced by a current density \mathbf{J} in a conducting volume \mathcal{D} , is given as

$$\mathbf{B}(\mathbf{r}, t) = \frac{\mu_0}{4\pi} \iiint_{\mathcal{D}} \mathbf{J}(\mathbf{r}', t) \times \frac{\mathbf{r} - \mathbf{r}'}{\|\mathbf{r} - \mathbf{r}'\|^3} dV', \quad (2)$$

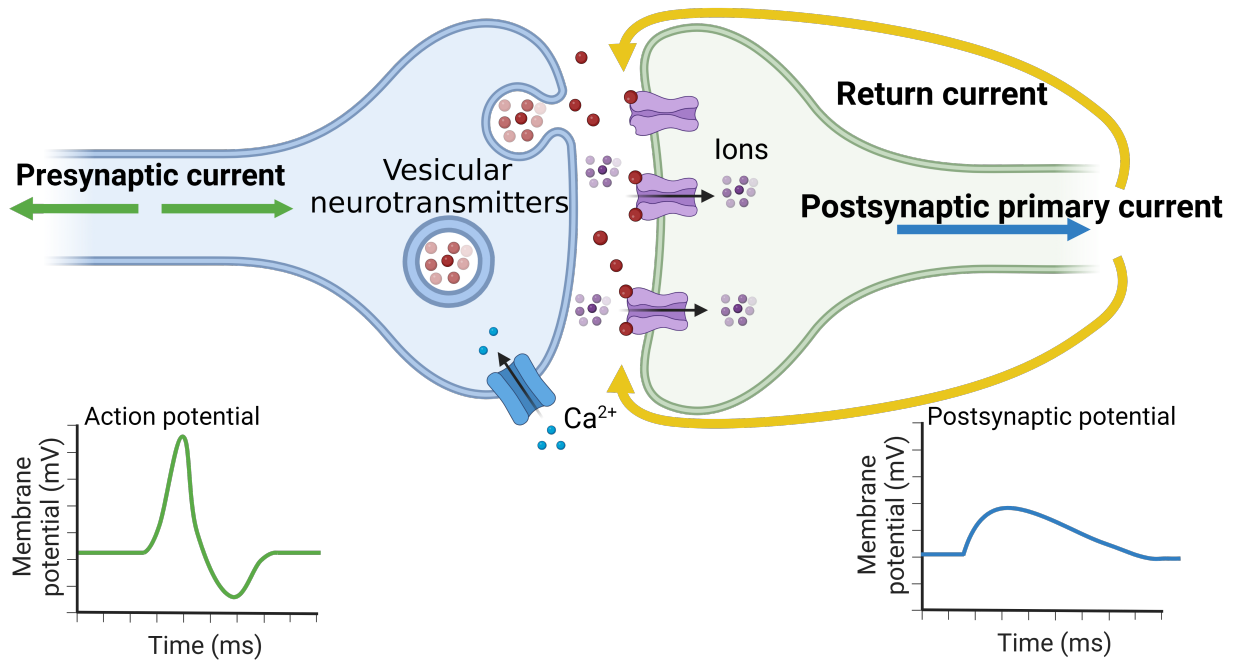
where μ_0 is the vacuum permeability and \mathbf{r}' is the location of the current in the brain. MEG measurements are performed using a combination of magnetometers and gradiometers respectively measuring the magnetic field magnitudes and their rate of change (gradient). Gradiometers are commonly divided into two different types with different spatial sensitivities: axial and planar gradiometers, both consisting of two magnetometers. Axial gradiometers are aligned orthogonally to the scalp and measure the change of magnetic flux along the radial direction. Planar gradiometers are placed tangentially to the scalp and measure the change in tangential components of the magnetic flux.

While MEG measures the extracranial magnetic fields induced by synchronous neural activity, EEG measures the respectively induced potential differences from the scalp. In a homogeneous medium with a conductivity of σ , the \mathbf{J}_p -induced potential at a point \mathbf{r} is given as

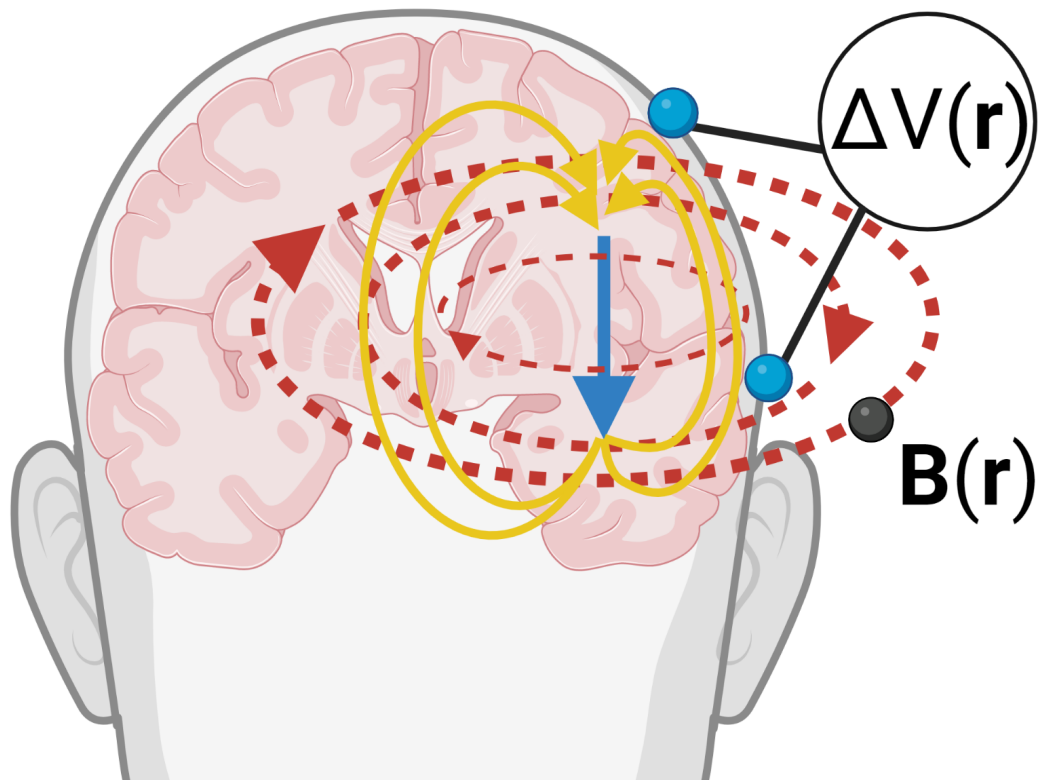
$$V(\mathbf{r}, t) = \frac{1}{4\pi\sigma} \iiint_{\mathcal{D}} \mathbf{J}_p(\mathbf{r}', t) \cdot \frac{\mathbf{r} - \mathbf{r}'}{\|\mathbf{r} - \mathbf{r}'\|^3} dV'. \quad (3)$$

However, in reality (in the case of a non-homogeneous medium), the EEG signal is substantially affected by the tissue conductivity -dependent volume currents \mathbf{J}_v . Due to the low and heterogeneous conductivities of tissues in the paths of EEG signals, the EEG signal is increasingly smeared before reaching the sensors, which causes uncertainties in EEG source modelling and is further assessed in this thesis. EEG is commonly performed using a scalp-fixed reference electrode at \mathbf{r}_{ref} , such that the measured signal at sensor i located at \mathbf{r}_i is the potential difference $\Delta V(\mathbf{r}_i) = V(\mathbf{r}_i) - V(\mathbf{r}_{ref})$ [12].

While the original physiological source \mathbf{J}_p of MEG and EEG signals is the same, the respective sensitivity patterns differ: MEG is sensitive toward intracellular primary currents and EEG is sensitive toward the extracellular volume currents (return currents) depicted in Figure 1. The differing sensitivities of MEG and EEG, and their consequences are further discussed in Section 2.1.3.



(a) Neurophysiological basis of the generation of the postsynaptic currents.



(b) Signal nature due to the postsynaptic primary current from Figure 1a above. MEG signal: Extracranial magnetic field $\mathbf{B}(\mathbf{r})$. EEG signal: Potential difference $\Delta V(\mathbf{r})$ at the scalp.

Figure 1: MEG and EEG signal generation. a) Generation of the postsynaptic currents due ion influx induced by the presynaptic action potential. b) Generation of MEG and EEG signals due to the induced postsynaptic primary current.

2.1.3 Sensitivities and complementary information

EEG and MEG measure cortical neural activity directly. Thus, M/EEG signals are able to represent distinct cortical activation patterns at millisecond-range temporal resolutions. Thus, EEG and MEG are commonly used in analyzing the timing and magnitude of cortical responses, for example, to aid in the assessment of cortical lesions [8, 15, 16].

The sensitivities presented in Section 2.1.1, are the main basis of the differences in the spatial resolution and in the sensitivity profile toward different post-synaptic current directions in MEG and EEG. Due to the volumetric flow of extracellular volume currents, EEG has a nearly homogeneous sensitivity pattern. In the case of MEG, however, the intracellular current -induced magnetic fields follow the Biot–Savart law, (see Equation 2) consequently causing a heterogeneous sensitivity pattern: insensitivity toward radial sources and sensitivity toward tangential sources. Hence, MEG is sensitive toward sulcular activity, such as activity in SII, which is located in the superior bank of the Sylvian fissure [1].

The skull is a poor conductor causing a distortive blurring effect in the EEG signal. Furthermore, there are intra- and inter-subject variabilities in skull structure which hinders cortical source localization when using EEG data [17, 18]. However, the skull does not substantially distort magnetic fields, which is the basis of the increased spatial resolution of MEG over EEG. Nonetheless, the development of the characterization of individual head models using anatomical magnetic resonance images (MRIs) and MEG data allows for the increased accuracy of EEG source localization [19, 20].

The differences in sensor sensitivities and subject-specific anatomy are taken into account in the construction of a lead field \mathbf{L} describing M/EEG signal projection from the sources to the sensors; the sensor-source sensitivity pattern. The signal m_i detected at sensor i is given by [12]

$$m_i(t) = \iiint_{\mathcal{V}} \mathbf{L}_i(\mathbf{r}') \cdot \mathbf{J}_p(\mathbf{r}', t) dV', \quad (4)$$

where the lead field $\mathbf{L}_i(\mathbf{r}')$ describes the sensitivity pattern of sensor i to a primary current at location \mathbf{r}' and \mathcal{V} is the measurement volume.

MEG and EEG measurements are performed such that the measurement-related signal-to-noise ratio (SNR) is maximized. Due to the weak magnitude of electrical neural responses, the induced magnetic fields are in the range of femtoteslas at the MEG sensors and are substantially weaker compared to other ambient magnetic fields. Thus, MEG measurements are performed in a magnetically shielded room, which is designed to mitigate the effect of the magnetic field of the Earth (in the μT range) and other external sources. The EEG measurement-related SNR is commonly dealt with careful subject preparation, most importantly, including the enhancement of the skin-electrode connections. Many MEG systems have an integrated EEG system; using a non-magnetic electrode cap allows the multimodal MEG–EEG measurement. The differing sensitivities of MEG and EEG give complementary information that can be used for improving the current and future subject-specific measurements and the reliability of measurement results [18, 20].

2.1.4 Current dipoles

While the nature of M/EEG signals differs, the spatiotemporal localization of the postsynaptic primary current is the focus in M/EEG signal analysis. A focal primary current source \mathbf{J}_p can be modelled as a current dipole representing location and orientation of neural activity, such that

$$\mathbf{J}_p(\mathbf{r}') = \mathbf{Q}\delta(\mathbf{r}' - \mathbf{r}_Q), \quad (5)$$

where \mathbf{Q} is the dipole moment, \mathbf{r}_Q is the location of \mathbf{J}_p if concentrated to a single point (dipole location), \mathbf{r}' is a location, and δ is the Dirac delta function [18]. By electrical conduction and the Biot–Savart law, a current dipole also induces a magnetic field. Accordingly, neural activity resulting from focal post-synaptic currents can be modelled with a current dipole by minimizing the difference between the dipole-induced topographical signal pattern and the respective measured data using least squares estimation (LSE), such that

$$\{\widehat{\mathbf{Q}}, \widehat{\mathbf{r}}_Q\} = \operatorname{argmin}_{\{\mathbf{Q}, \mathbf{r}_Q\}} \|\mathbf{m} - \widehat{\mathbf{m}}\|^2, \quad (6)$$

where \mathbf{m} is the measured signal vector (EEG or MEG) and $\widehat{\mathbf{m}}$ is the signal vector induced by the current dipole. The current dipole with location $\widehat{\mathbf{r}}_Q$ and moment $\widehat{\mathbf{Q}}$ is called as the equivalent current dipole (ECD).

Due to the direct nature of dipole modelling, sources of interest that are temporally or spatially, or both, adjacent, may smear the induced M/EEG signal patterns of each other, and thus may not always be easily localized without assigning prior source or sensor space information. Furthermore, dipole fitting becomes less reliable in the case of weaker sources of interest due to leakages from other active nearby non-interesting sources. Hence, dipole fitting is most efficiently used in modelling initial early evoked brain activity; for secondary responses appearing at longer latencies, additional steps in data processing are commonly required.

2.1.5 Inverse problem and minimum-norm estimation

M/EEG sensor space data \mathbf{m} can be computed from a discrete source distribution \mathbf{s} using a system of linear equations,

$$\mathbf{m} = \mathbf{L}\mathbf{s} + \mathbf{n}, \quad (7)$$

where \mathbf{L} is the forward operator – the so-called lead field matrix, describing signal projections from the sources to the sensors, and \mathbf{n} is the measurement noise.

The number of sources in the brain is substantially more compared to the number of used sensors. Consequently, when a limited number of sensors, *i.e.* measurement channels, is used to measure neurally induced fields, the sources in the brain can not be independently characterized. Thus, solving the underlying source distribution \mathbf{s} is an ill-posed problem of linear equations, and thus does not have a unique solution. However, different linear inverse modelling methods have been introduced for computing an estimate $\widehat{\mathbf{s}}$ for the source distribution, such that

$$\widehat{\mathbf{s}} = \mathbf{W}\mathbf{m}, \quad (8)$$

where \mathbf{W} is the inverse operator, which can be created using the measured data and other prior information [21].

For a dynamic system, such as the brain, multicollinearity across sources is likely. The effect of multicollinearity can be partially countered by using Tikhonov regularization providing a tolerable bias-variance trade-off in model parameter estimation, and consequently, increased efficiency in independent source extraction [22, 23]. L2 minimum-norm estimation (MNE) is a method for estimating the underlying source distribution by simultaneously minimizing the L2 norm of both the estimated source currents $\|\hat{\mathbf{s}}\|^2$ and the residuals $\|\mathbf{m} - \mathbf{L}\hat{\mathbf{s}}\|^2$ between the measured and predicted data. The method is based on the assumption that without prior knowledge, the most probable brain state has the least amount of energy; the aim is to find the source current distribution $\hat{\mathbf{s}}$ with the smallest norm that induces the best estimate of the measured signals \mathbf{m} [18, 24]. Assuming that the measurement noise \mathbf{n} and the source distribution \mathbf{s} are normally distributed with zero mean, the general form of the MNE inverse operator is written as [24, 25, 26]

$$\mathbf{W} = \mathbf{R}\mathbf{L}^T(\mathbf{L}\mathbf{R}\mathbf{L}^T + \lambda^2\mathbf{C})^{-1}, \quad (9)$$

where λ is the Tikhonov regularization parameter, and \mathbf{R} and \mathbf{C} are the data and noise covariance matrices, respectively.

2.2 Principles of transcranial magnetic stimulation

Transcranial magnetic stimulation (TMS) is a non-invasive brain stimulation method where rapidly changing strong magnetic fields are used to excite brain activity [10, 11]. The magnetic fields are delivered to the cortex using a specifically designed coil as visualized in Figure 2a.

The magnetic field \mathbf{B} at location \mathbf{r} and time t , are induced by strong current pulses $I(t)$ in the TMS coil and follow the Biot–Savart law as

$$\mathbf{B}(\mathbf{r}, t) = \frac{\mu_0}{4\pi} I(t) \oint_{\mathcal{C}} \frac{d\mathbf{l}(\mathbf{r}_c) \times (\mathbf{r} - \mathbf{r}_c)}{|\mathbf{r} - \mathbf{r}_c|^3}, \quad (10)$$

where μ_0 is the vacuum permeability, \mathbf{r}_c is the location of the current and \mathcal{C} is the path of the current in the TMS coil.

By Faraday’s law of induction, a time and location dependent magnetic field \mathbf{B} will induce an E-field \mathbf{E}_p in the surroundings (in this case, in the brain matter) defined by

$$\nabla \times \mathbf{E}_p(\mathbf{r}, t) = -\frac{\partial \mathbf{B}(\mathbf{r}, t)}{\partial t}. \quad (11)$$

Due to the primary E-field \mathbf{E}_p and the heterogeneous conductivities in brain tissue, a charge density $\rho(\mathbf{r}, t)$ is accumulated at tissue boundaries inducing a scalar potential secondary E-field \mathbf{E}_s following Gauss’ law as

$$\nabla \cdot \mathbf{E}_s(\mathbf{r}, t) = \frac{\rho(\mathbf{r}, t)}{\varepsilon_0}, \quad (12)$$

where ε_0 is the vacuum permittivity. Both the primary and secondary E-fields act as stimulating factors. Thus, the total stimulating E-field is defined as

$$\mathbf{E} = \mathbf{E}_p + \mathbf{E}_s. \quad (13)$$

The TMS-induced electric field interacts with charged particles, and consequently, axons, in the brain. Axons are myelin sheath covered slender projections that are responsible for conducting inter-neuronal information in the form of action potentials. The myelin sheath provides the axon with insulation due to its lipid-rich nature enabling high transverse resistance and a low electrical capacitance. Negatively charged ions move against the induced E-field in brain matter. While the negative ions are not able to penetrate the insulating myelin sheath of axons, they are able to indirectly interact with positively and negatively charged ions in the axon by electric charge interaction as shown in Figure 2b. The positive and negatively charged particles in the axon are respectively drawn to and repelled by the negative ions on the other side of the myelin sheath inducing a depolarized potential difference in the axon, resulting in possible action potential initiation.

The magnitude of the neuronal response to TMS is highly dependent on the magnitude of the applied magnetic field and the relative orientations of the induced E-field and the axons of the targeted neuronal cluster. If the E-field is parallel to an axon, no axonal depolarization is induced. On the contrary, perpendicular E-field and axon orientations incite global axonal depolarization; it is thought that the strongest stimulatory effect is incited at axon curves or terminations of especially layer V pyramidal neurons [11, 27].

TMS applications range from studying inter-areal connectivity by evoking cortical activity or inducing temporary lesions to the clinical treatment of various neurological diseases [28, 29]. However, due to individual differences and the vastly heterogeneously clustered nature of neurons, and consequently, axons, in the brain, there is a lack of understanding about the stimulated cortical spot and the stimulation intensity at the target area. Hence, navigated TMS (nTMS) has been developed for accurate localized electromagnetic induction in the cortex with on-site online adjustments [30]. Furthermore, nTMS is a non-restrictive addition to other TMS modalities and is thus commonly utilized in aiding TMS experiments.

Simultaneous TMS measurements, such as TMS-EEG, can be performed due to the progression of neuronavigation, signal processing techniques, and the development of TMS-compatible hardware [11, 30]. Combining TMS and EEG is a prevalent method in studying inter-areal effective connectivity [31]. However, due to the strong magnetic fields used in TMS, simultaneous TMS and MEG has not been efficiently practiced. Nevertheless, MEG provides a good combination of both spatial and temporal resolutions, and thus can provide accurate information on the timing and source of neural responses, which can be used as prior information in neuronavigation and in the assessment of TMS-evoked potentials (TEPs).

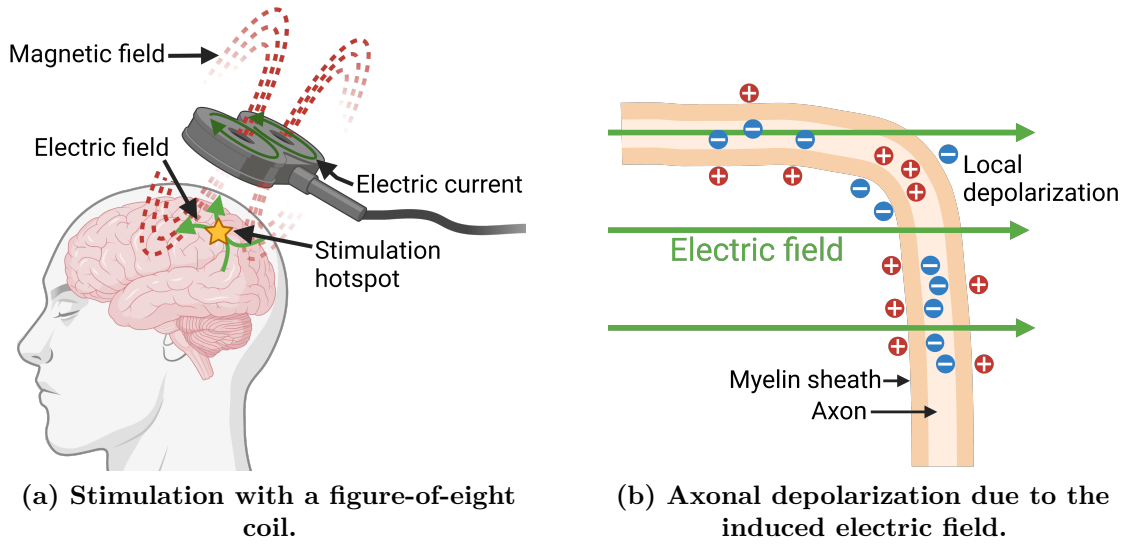


Figure 2: Methodological representation of transcranial magnetic stimulation. a) Electrical current flow in the TMS-coil induces a magnetic field that induces an electric field in the cortex. The electric field is maximized at the stimulation hotspot located under the center of the figure-of-eight coil. b) Charge density accumulation at axon boundaries and resulting depolarization due to the induced electric field. Sufficient membrane depolarization results in the firing of an action potential.

2.3 Somatosensory system

The somatosensory system is responsible for processing somatosensory stimuli including temperature, nociception (sense of pain), proprioception (sense of bodily position), and tactile information. The somatosensory cortex is the main cortical somatosensory processing unit and is divided into two functional anatomical areas: the primary (SI) and secondary (SII) somatosensory cortices. This section presents the anatomical and functional divisions due to somatosensory pathways, the responses and lesion studies of SI and SII, and introduces how somatosensory activity has been previously measured with MEG and EEG.

2.3.1 Primary somatosensory cortex

SI is the primary processing unit of bodily sensation. SI is located in the postcentral gyrus of the parietal lobe and is functionally divided into Brodmann areas (BAs) 1, 2, and 3, which is subdivided into areas 3a and 3b. Generally, BAs 1 and 3a respond to cutaneous tactile input and BAs 3a and 2 to proprioceptive input, while BA 3b is the main reflector of somatotopic activity [4, 32].

Below the neck sensory information from the skin, joints and muscles is relayed to SI via their respective somatosensory pathways depending on the type and intensity of the somatosensory stimulus. Receptors of somatosensory neurons are responsible for transducing physical sensory input into action potentials. The initiated action potential travels via the

dorsal root ganglion to the spinal cord and synapses with the spinothalamic tract, which as the name suggests, synapses in the thalamus. Somatosensory relays in the thalamus are located in the ventral posterior nucleus, from which the respective sensory pathways finally radiate to SI. An illustration of somatosensory pathways is presented in Figure 3a.

The bodily location of the somatosensory stimulus affects the length and travelled pathway of the somatosensory signal. The closer the stimulus is to the somatosensory cortex and the thalamus, the more efficient it is to bypass the extracephalous parts of the somatosensory pathway. For example, the neural signal arising from the touch of the cheek will travel directly to the thalamus and further relay to SI.

SI has been found to activate contralaterally to stimuli below the neck. That is, below the neck somatosensory information gained from either hemisphere of the body will be relayed to the contralateral SI. For sensations upward from the neck, the sensory signal travels via the trigeminal cranial nerve system, which commonly projects to the ipsilateral side [33]. However, contralaterally dominant bilateral activation patterns measured with EEG have been reported in studies stimulating trigeminal nerves of the face [34, 35]. The topological arrangement of somatic senses is preserved in the somatosensory pathways [36]. Consequently, SI is symmetry-somatotopically divided across hemispheres, pictorially represented by the sensory homunculus in Figure 3b below.

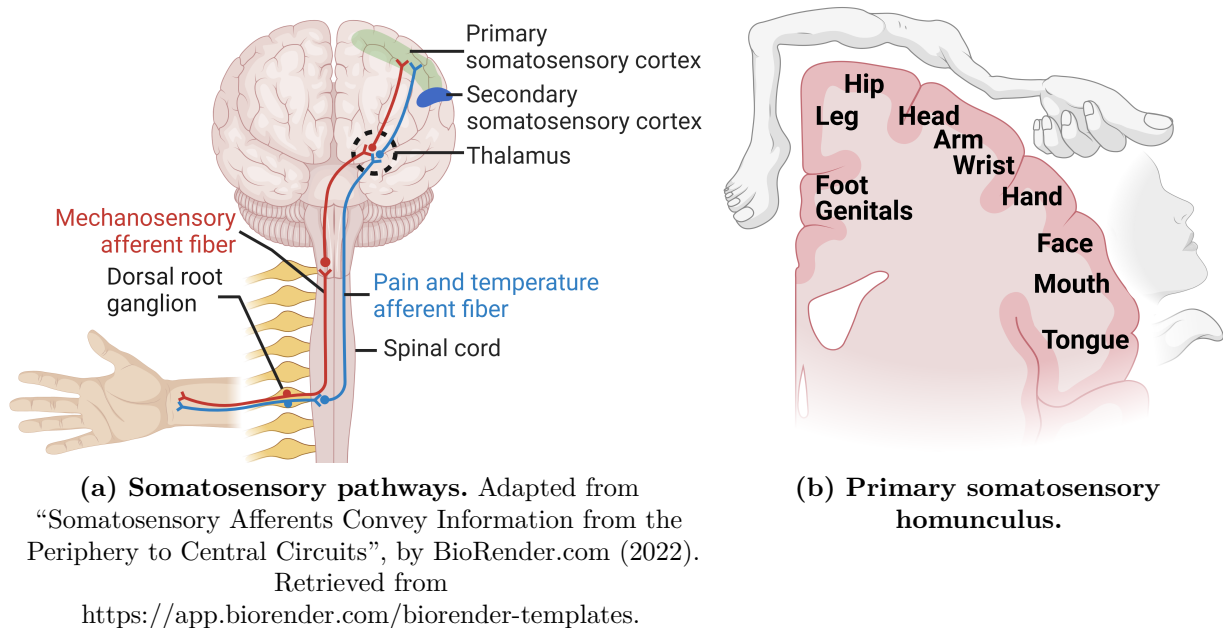


Figure 3: Organisation of the somatosensory system. a) Somatosensory pathways relaying information due to somatosensory stimuli below the neck. b) Primary somatosensory homunculus-represented functional areas.

Feedforward SI projections synapse, for example, in the primary motor cortex, which supports the crucial role of SI in sensorimotor integration [37, 38]. Additionally, SI is

interconnected with other primary sensory cortices (for example, the visual and auditory) and is thus an integral factor in multisensory interplay [38, 39].

2.3.2 Activation patterns of the primary somatosensory cortex

The activation patterns of SI are commonly studied using peripheral nerve stimulation (PNS), for example MNS, of the upper extremity, most commonly, the fingers or the wrist [4, 6]. The initial activation of the somatosensory cortex arises at the respective stimulus-site somatotopic area in the contralateral SI after approximately 20 ms due to PNS, and is termed the N20 response (negative response after approximately 20 ms after the stimulus onset). N20 represents initial excitatory postsynaptic potentials and is hence a common area of focus when studying the somatosensory cortices using MEG and EEG [4, 6, 7]. Additionally, the N20 response has clinical significance as even small time delays over 20 ms can indicate lesional abnormalities [40].

Other SI responses within 100 ms evoked by PNS include the P35 (positive inhibitory postsynaptic potential after approximately 35 ms due to stimulus onset), N45, and P50/60/75 responses that also arise at the respective somatotopic area. However, the exact locations and individual prevalences of the responses differ. For example, the N20 response arises closer to the inner skull boundary compared to the commonly stronger P35 response, and the N45 and P35 responses are respectively enhanced and weakened when short interstimulus intervals (ISIs) are used [6, 41]. An example of a SI waveform with prevalent SEF-components over a representative parietal MEG sensor is presented in Figure 4. A typical N20 dipole is presented in Figure 5.

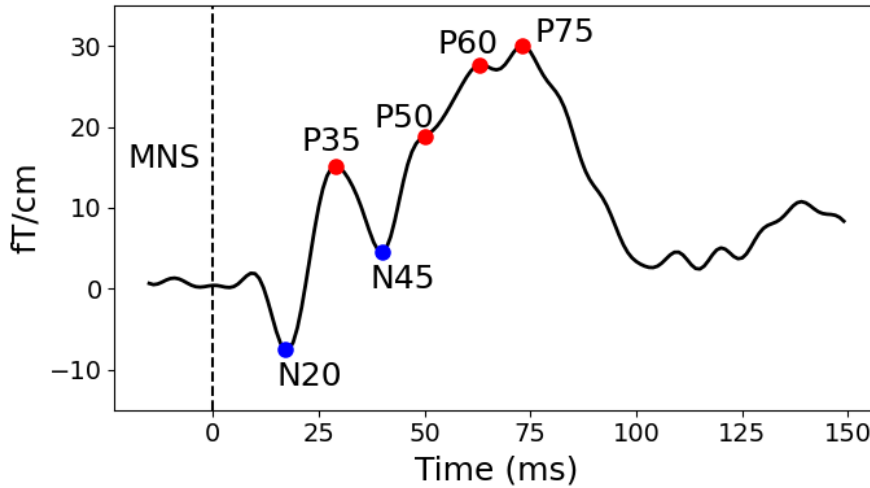


Figure 4: An averaged right SI waveform over gradiometer MEG2312 with marked prevalent SEF components. The activity was evoked by electrical MNS at the left wrist at $t = 0$ ms with an ISI of 3 s.

2.3.3 Secondary somatosensory cortex

SII adjoins SI at the ceiling of the lateral sulcus and is located in the parietal operculum. The structure of SII is mainly represented by cytoarchitectonic areas OP1 and OP4, roughly corresponding to the functional parietal ventral (PV) and S2_{sub} areas. As in the case of SI, (however, not as accurately defined) the functional behaviour of SII has mirror-like somatotopic divisions with representations of the head, hands, and feet at the boundary of PV and S2_{sub} [42, 43].

SII is believed to be responsible for tactile object recognition and memory-related processing of somatic sensations [1]. SII has anatomical connections to the hippocampus and amygdala, which further supports the role of SII as a plastic modulating sensory memory storing unit [2]. Furthermore, contrary to SI, the responsiveness of SII is bilateral due to unilateral stimuli, which supports the practical convention of unilateral training enhancing bilateral sensorimotor performance.

SII has been found to activate 70–90 ms (P100 response) after the initial N20 response in SI when ISIs of over 1 s are used [6] with small inter-hemispherical time lags [4, 6, 8]. The activation patterns of SII, along with SI, have found to be significantly related to the perceived intensity of pain [2, 3]. Additionally, left-hemisphere-dominant SII activation patterns have been found due to bilateral electric MNS indicating handedness-independent functional specialization of SII [44, 45]. These findings suggest that while SII is bilaterally nearly simultaneously activated, the response magnitudes differ hemispherically due to the nature of the stimuli. An example of typical P100 dipoles is presented in Figure 5.

While the nature of connectivity between SI and SII has not been unravelled, the activation patterns of SI and SII due to PNS and nociceptive stimuli suggest relations of both SI and SII, possibly enabled by SI–SII connectivity, in somatosensory interplay.

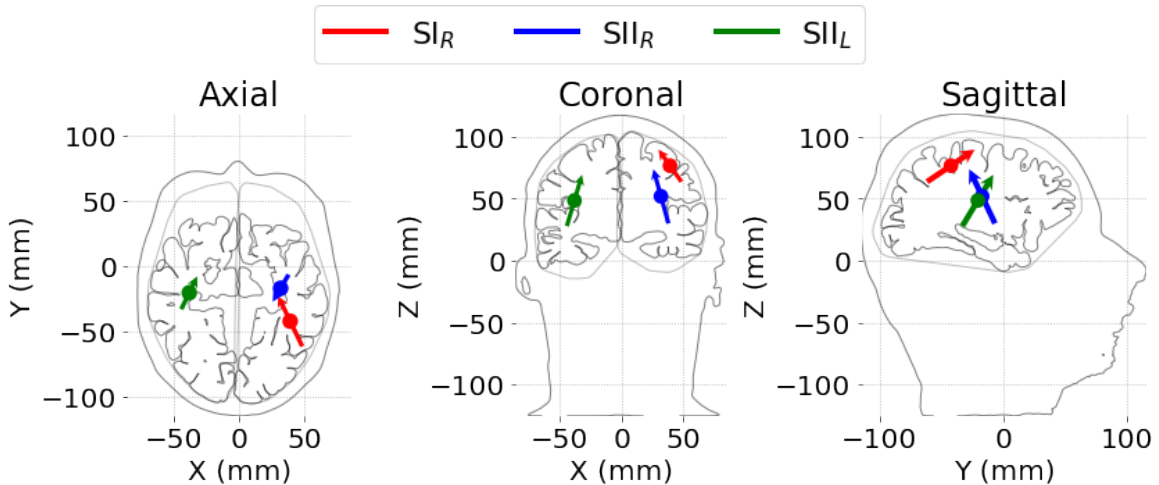


Figure 5: Exemplar SI_{Right} (N20) and SII_{Right/Left} (P100) dipoles. The dipoles represent initial activity in SI and SII evoked by electrical MNS at the left wrist. The dipole locations have been slightly adjusted for better visualization.

2.3.4 Somatosensory lesions

Multiple neuropathic and developmental neurological diseases, such as parasthesia, hyperalgesia, tactile agnosia, and Parkinson’s disease, are correlated with significantly differing somatic responses compared to neurotypicals in the somatosensory cortex [46, 47, 48]. The prevalence of chronic pain with neuropathic features has been estimated to affect 7–8% of the general population and is correlated with mood disorders and hormonal imbalances [49, 50, 51, 52]. The somatosensory cortex has shown to be a central factor in emotion processing and in modulation of nociceptive stimuli with cognitive and emotional factors [53, 54, 55, 56]. Consequently, both the affects and development of abnormal somatosensory activity and mood disorders are positively correlated leading to further poorer prognosis for those suffering from both disorders [57].

Lesions in the somatosensory pathway are commonly caused by spinal injuries or neuropathic diseases (for example, due to a stroke) and are commonly depicted as the inhibition of unilateral perception and somatosensory processing of somatosensory information [8, 9]. In patients with right-hemispherical strokes, the activation of the ipsilateral SII has been shown to be absent while the responsiveness of the contralateral SII remained prevalent. The modified activation patterns suggest direct ipsilateral SI–SII feedforward connectivity and that the contralateral SII receives information from the peripheral nervous system via thalamocortical pathways without the intervention of SI [8]. A respective decrease and preservation of SI and SII responsiveness has been observed in patients with a thalamic stroke when compared to the contralesional hemisphere, which suggests direct parallel thalamocortical relays to SII or re-organizational processes of damaged neural pathways [9]. With functional MR-imaging utilizing tactile and nociceptive stimuli, thalamocortical pathways to the contralateral SI and SII, and ipsilateral bidirectional pathways between SI and SII, have been observed, which suggests a parallel processing structure between SI and SII [58]. However, due to the limited temporal resolution of functional MR-imaging [59], the temporal scale of parallel processing can not be determined. In [58], distinct corticothalamic feedback connections from SI and SII are also suggested, which may constitute to the activation of the contralateral hemisphere.

The plastic roles of both somatosensory cortices, the healthy nature of bilateral activation, and memory-related processing of SII suggest the role of SII being an integral factor in somatosensory diseases and a necessary target alongside SI in respective clinical research.

3 Methods

This section presents the relevant methods applied in measuring, processing, and analyzing the MNS–M/EEG and TMS–EEG evoked responses in SI and SII. The general methodological steps are presented in Figure 6 below.

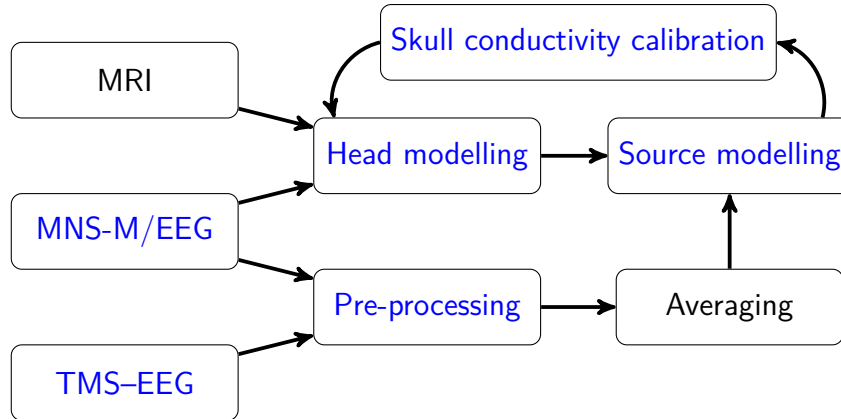


Figure 6: Methodological pipeline. Arrow directions represent the methodological order.

3.1 Experiment

The purpose of the experiments was to assess the nature of the pathways between SI and SII. The experiment was designed for the comparison of evoked responses in SI and SII due to peripheral MNS and central TMS. With TMS, SI can be stimulated directly without activating the natural high-order thalamic pathways to SI. Thus, stimulating SI alone provides essential information about the possible direct or indirect pathways between SI and SII when compared to responses evoked by peripheral stimuli activating the natural somatosensory pathway (see Figure 3a), including SI and SII. The possibly activated pathways due applied stimulus between SI and SII are depicted in Figure 7 below.

The experiments were done by measuring seven right-handed subjects (six men and one woman) with ages of 24.1 ± 3.4 years (mean \pm standard deviance (SD)), each participating in both MNS–M/EEG and TMS–EEG measurements. Those subjects who did not have anatomical T1- and T2-weighted MRIs available underwent the respective measurements at the Aalto NeuroImaging (ANI): Advanced Magnetic Imaging (AMI) Centre. The protocol for the MNS–M/EEG and TMS–EEG measurements is presented in Table A1. Each subject gave a written consent to participate in the experiment. The implementation of the project and the measurement protocol was approved by the Aalto University Research Ethics Committee. This thesis also includes the analysis of a pilot subject (Subject 1), where the measurements were performed prior to the ethical permit with a slightly differing MNS–M/EEG protocol; see Appendix A for more information.

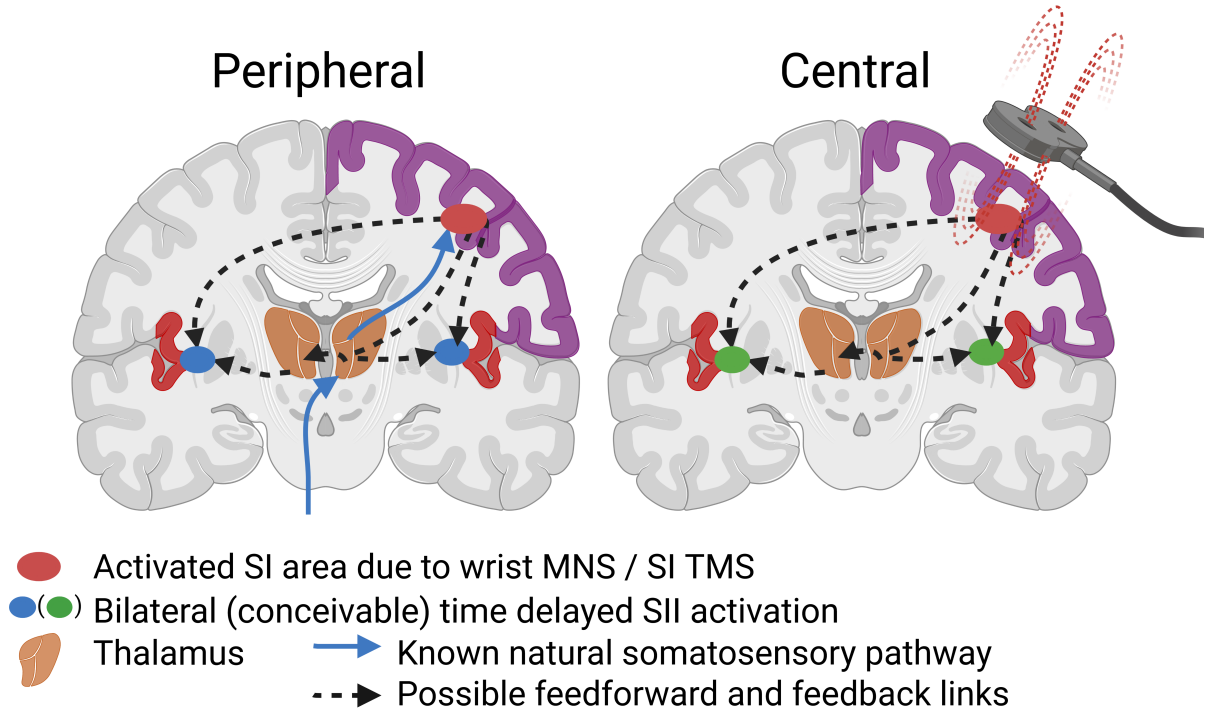


Figure 7: Depiction of possibly activated pathways between SI and SII. Peripheral (left): electric MNS at the left wrist. Central (right): TMS targeted at the right-hemisphere SI.

3.1.1 Magneto- and electroencephalography

The participants were in a seated position with the left hand and forearm relaxed. Electrical MNS with 3-s interstimulus intervals (ISIs) was applied via stimulation electrodes attached to the left wrist. The used stimulation intensity was 150% of the respective resting motor threshold (rMT). The rMTs (Mean \pm SD: 7.8 ± 1.3 mA) were defined as the minimum stimulation intensity that produced visible movement of the left thumb.

The data were recorded with the MEGIN TRIUXTM neo 306-channel (102 magnetometers and 204 gradiometers) MEG device in the ANI MEG Core infrastructure in a magnetically shielded room with a sampling rate of 1000 Hz. The measurements were divided in to three blocks each composed of 100 stimuli. EEG was measured with a built-in 32-channel system, following a standard 10–20 layout. The EEG reference electrode was close to the vertex and the head position indicator (HPI) coils were mounted to designed locations on the EEG cap. Bipolar electrooculogram (EOG) electrodes were applied to areas under and over the eyes of the subject for detecting vertical and horizontal ocular activity. The ground electrode was attached to the left arm of the subject near the stimulator to mitigate MNS-artifacts. Five HPI coils were used for continuous head position monitoring during the measurement, and over 100 points were used to digitize the head of the subject. The EEG electrode positions

were also digitized.

3.1.2 Transcranial magnetic stimulation

The participants were in a seated legs elevated position with the left hand and forearm relaxed. The magnetic stimuli (120 or 90% rMT; see Appendix A) were targeted to the individually localized activated SI area from MEG data, with the help of an individual-MRI-calibrated neuronavigation system. Due to TMS-evoked muscular artifacts, the stimulation target had to be adjusted to ensure good SNR due to SI stimulation. The rMTs (Mean \pm SD: $47.4 \pm 5.2\%$ of the maximum stimulator output) were defined as the minimum stimulation intensity that produced a motor evoked response in the left abductor pollicis brevis muscle (IAPB), of over $50 \mu\text{V}$ in over 50% of 20 trials (Subjects 1–3) when stimulating the motor hotspot. For Subjects 4–7, an automated rMT defining algorithm provided in the stimulation system was used. The motor hotspot was defined as the location in the motor cortex resulting in the best extracted movement of the left thumb.

The measurements were performed at the Advanced Brain Stimulation Laboratory at the Department of Neuroscience and Biomedical Engineering at Aalto University. The data were recorded with the Bittium NeurOne™ TMS-compatible EEG system using 62 EEG channels, following a standard 10–20 layout, and with a sampling rate of 5000 Hz. The reference and ground electrodes were respectively attached behind the left ear and to the skin surrounding the left cheekbone of the subject. The measurements were divided in to three blocks composed of 100 biphasic stimuli with a mean ISI of 2.15 s (randomized between 2.0 and 2.3 s). The navigation and delivering of the stimuli were performed with the Nexstim Navigated Brain Stimulation (NBS 5) System. All EEG-electrode positions were digitized. Noise masking was used to suppress auditory responses otherwise evoked by the clicking sound of the TMS coil.

3.2 Pre-processing

M/EEG signal pre-processing is an essential step in improving signal quality prior to analysis. However, due to the differing physical nature of MEG and EEG signals, and the used measurement system, the approach in pre-processing also differs. Furthermore, TMS–EEG data requires supplementary steps compared to the conventional EEG pre-processing pipeline due to the additional artifacts elicited by the TMS pulse. This section presents the general steps applied in M/EEG and TMS–EEG pre-processing. The respective pipelines are presented in Figure 8.

Signal space separation (SSS) in the form of Maxwell filtering with continuous head movement compensation and the identification and reconstruction of bad static MEG channels was performed with the Maxfilter software 2.2 (MEGIN Oy, Helsinki, Finland). Other M/EEG data pre-processing steps were performed with the MNE-Python software [60]. For MNS–EEG data, the reconstruction of bad EEG sensors was performed using spherical spline interpolation. TMS–EEG data pre-processing were performed with the EEGLAB software using the TESA toolbox [61, 62, 63]. All data were band-pass filtered

from 1 to 100 Hz and powerline noise was filtered near 50 and 100 Hz (MNS-M/EEG: a zero-phase notch filter with a 1-Hz transition bandwidth and TMS-EEG: band-stop filters at 48–52 and 98–102 Hz). Stimulus artifact removal was performed using windowed interpolation.

Independent component analysis (ICA) is a method for extracting statistically independent signals from a multivariate signal distribution [64]. ICA was used to detect ocular artifacts and to enhance the MNS-artifact removal. Artifactual epochs were identified manually and rejected from further analysis. Additionally, in TMS-EEG data, noise suppression was enhanced with the source-estimate-utilizing noise-discarding algorithm (SOUND) and muscular artifacts were suppressed using the signal-space projection and source-informed reconstruction algorithm (SSP-SIR) [65, 66]. SOUND utilizes MNE to cross-validate data between the sensors for suppressing artifacts and noise [65]. SSP-SIR projects out TMS-evoked muscle artifacts using SSP and utilizes MNE to estimate the source distribution in the brain. The source distribution is mapped back to the sensor space and is used to interpolate the information in the rejected sensors [66].

While downsampling is also commonly applied in MEG analysis, here downsampling was only applied to TMS-EEG data to set the sampling rates (1000 Hz) to be identical for the TMS-EEG and MNS-M/EEG data for accurate temporal comparisons of the responses. Downsampling was applied as the last step in TMS-EEG pre-processing to mitigate the effect of filtering artefacts. Evoked responses due to both stimulus modalities are represented by the averages of the respective pre-processed epochs.

Pre-processing pipelines

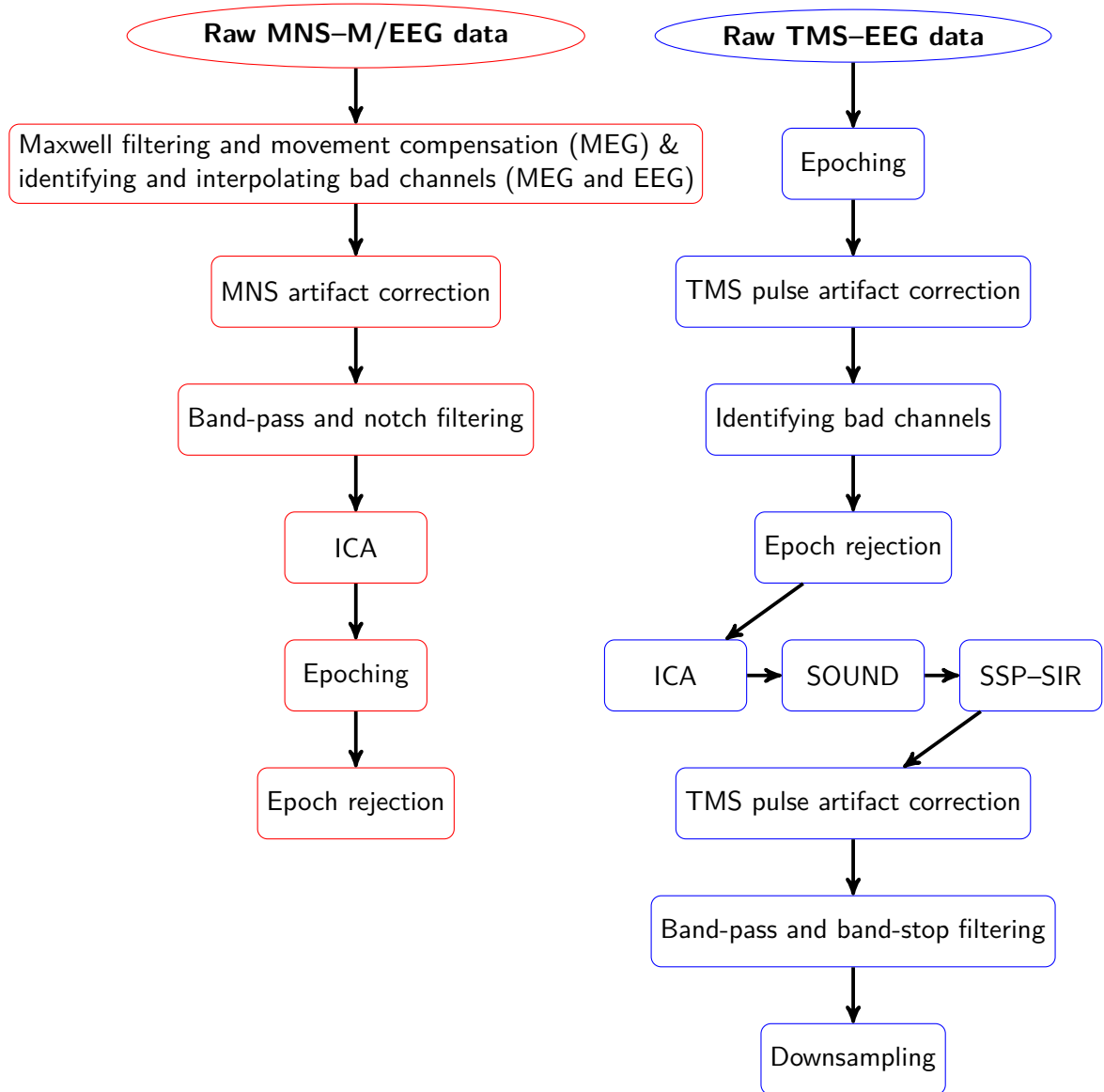


Figure 8: General pipelines used in MNS-M/EEG and TMS-EEG data pre-processing. ICA: Independent component analysis, SOUND: Source-estimate-utilizing noise-discarding algorithm, and SSP-SIR: Signal-space projection and source-informed reconstruction.

3.3 Head modelling

Individual cortical reconstructions were performed using both T1- and T2-weighted MR images using the FreeSurfer software [67]. Reconstructions were performed primarily using T1-weighted images while T2-weighted images were used for increasing the fidelity of the pial surfaces for enhancing the accuracy of the EEG forward model. Head models used in analysis were done with the boundary element method (BEM) and the BEM grade 4 icosahedral surfaces (brain, inner skull, outer skull, and outer skin) were created with the FreeSurfer watershed algorithm [68]. The M/EEG-MRI co-registration was performed with the MNE-Python software using high-resolution head models [60].

The skull does not substantially distort magnetic fields, thus, one-layer BEM models were used in MEG source modelling. However, in analyzing the TMS-EEG data, three-layer BEM models (without the inclusion of the cerebrospinal fluid) were used with individually calibrated skull conductivity values as described below.

Skull conductivity calibration

As discussed in Section 2.1.3, the poor conductivity of the skull induces the smearing of EEG signals, and thus has a substantial effect on combined MEG-EEG and EEG source analysis [19]. Hence, optimizing the varying values of conductivity for the individual head models (in this case, three-layer BEM models) can improve the accuracy of EEG source modelling [69]. In this thesis, realistic skull conductivity parameters were computed for subject-specific volume conductor models using respective MEG- and EEG-based somatosensory evoked fields and potentials (SEFs and SEPs) from the multimodal MNS-M/EEG -measurement.

While all tissue conductivities have an effect on head modelling for EEG, optimizing the weakest individual conductivity component – the conductivity of the skull, has the most substantial effect on accurate individual head model calibration and source localization [70]. Thus, for reducing complexity and enhancing computational efficiency, the brain and scalp were set to have constant equal conductivities of $\sigma_{\text{brain}}, \sigma_{\text{scalp}} = 330 \text{ mS/m}$, which are realistic for such tissues [69]. The charge density accumulation at tissue boundaries depends on the relative conductivities of the tissues. Thus, in the calibration procedure presented below, the possible conductivities of the skull $\sigma_{\text{skull},n}$ were given as fractional values of the conductivities of the brain and the scalp. The method is adapted and modified from [20], and the basis is to find such values of skull conductivity that result in the best head model giving the most accurate EEG topography -estimate induced by dipolar activity fitted sequentially to SEF and SEP data. The accuracy was determined with the Goodness of Fit (GoF); see Section 3.7. Due to variabilities in skull conductivity and multiple candidate SEP topographies, it is recommended to use multiprocessing, saving the created head models, and to use an initial large step size ($\sigma_{\text{skull},n} - \sigma_{\text{skull},n+1}$) for computational efficiency. For specifications in dipole fitting, see Section 3.4.1 and Appendix B.

Skull conductivity calibration using somatosensory evoked fields and potentials

1. Inspect and pick a SEF/SEP topography that is elicited as a dipolar activation pattern. Let this topography be called $(\cdot)_{\text{pick}}$. Prioritize SEP topographies in selection.
2. Define a set of triplets $\Sigma = \{(\sigma_{\text{brain}}, \sigma_{\text{skull},1}, \sigma_{\text{scalp}}), \dots, (\sigma_{\text{brain}}, \sigma_{\text{skull},k}, \sigma_{\text{scalp}})\}$ corresponding to layer-wise conductivity values for the brain, skull and scalp. Order the skull conductivity values such that $\sigma_{\text{skull},n} > \sigma_{\text{skull},n+1}$.
3. For each conductivity triplet:
 - (a) Construct a three-layer BEM head model.
 - (b) Fit a dipole D_F to SEF_{pick} . Save the location \mathbf{r}_F of D_F .
 - (c) Fit a dipole D_P with a fixed location \mathbf{r}_F to SEP_{pick} . Save the orientation \mathbf{o}_P of D_P .
 - (d) Use D_P , D_{F2} or D_F (see step 4) to estimate SEP_{pick} .
 - (e) Calculate the residuals by calculating the difference between the measured and estimated SEP topographies; see Figure 9.
 - (f) Calculate the GoF.
4. Inspect the values of GoF and pick the skull conductivity corresponding to the highest GoF:
 - (a) If GoF reaches a clear non-convergent maximum, pick the skull conductivity resulting in D_P corresponding to the to highest GoF.
 - (b) If GoF does not reach a clear maximum, return to step 3 and estimate SEP_{pick} with a fixed dipole D_{F2} with location \mathbf{r}_F and orientation \mathbf{o}_P fitted to SEF_{pick} .
 - (c) If GoF still does not reach a clear global maximum with D_{F2} , return to step 3 and estimate SEP_{pick} with D_F .
5. Optional: Let Σ_q be the picked triplet (q^{th} component in Σ). Return to step 3 with a new set of triplets and a smaller step size, such that $\Sigma_{\text{new}} = \{\Sigma_{q-1}, \dots, \Sigma_{q+1}\}$ to gain a higher accuracy.

The algorithm was created for the use of accurate head modelling for TMS–EEG source modelling. Hence, the EEG signal was utilized in the algorithm as much as possible. The SEF-component was used as the spatial locator for the dipole due to the superior spatial resolution of MEG over EEG. In turn, EEG has a differing sensitivity pattern, and thus, the SEP topography was used to initially determine the dipole orientation and magnitude. However, due to the dynamic relationship between the fitted dipole magnitude and skull conductivity, inappropriately low values of skull conductivity may result in spuriously high dipole magnitudes, while still resulting in a high but converging GoF. Hence, the underlying source strength is calculated as: 1. As the magnitude of the location-fixed dipole fitted to SEP data. 2. If GoF converges and does not produce a reliable maximum: as the magnitude

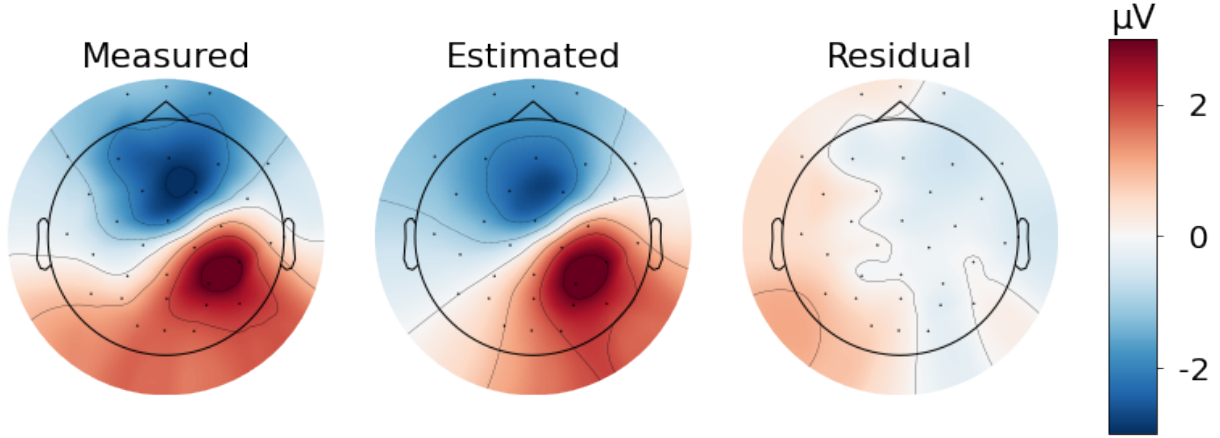


Figure 9: Example of the measured, estimated, and residual SEP topographies. The estimated topographical signal pattern was induced by a P35 dipole (with GoF $\approx 96\%$) in a head model with $\sigma_{\text{skull}} \approx 6.9$ mS/m.

of a SEF-fitted fixed dipole with a location and orientation respectively defined by the dipoles fitted sequentially to SEF and SEP data. 3. If the estimated source orientations differ substantially resulting in spurious results: the SEP topographies were estimated with the original dipole fitted to SEF data. The possible spuriousities in dipole magnitudes and orientations were taken into account in step 4 of the algorithm such that the EEG signal is iteratively given less prevalence if no reliable GoF maximum is found.

Due to inter-subject variabilities in the somatosensory responses and the use of a 32-channel EEG system, there were large differences in the measured SEP topographies. Optimally, the skull conductivity would be assessed using the N20 response due to less background brain noise. However, the early N20 SEP topographies were weak, smeared (non-dipolar; see Figure 11), and thus, the corresponding dipoles could not be efficiently used. Thus, for each subject, the dipolar P35 response was used as the SEF/P component in the calibration procedure. The used SEP topographies were picked based on their dipolar nature with visual inspection, which did not always match the peaks of global field amplitude. For example, the P35 response reaching its maximum amplitude at 35 ms post-stimulus may produce a relatively reliable dipolar activation pattern but a weaker topography corresponding to the same response at 33 ms may still be more dipolar in nature. Other responses, such as P50, were also used in testing the calibration procedure and produced similar results for some of the subjects, but the use of P35 produced the most reliable results overall in terms of maximizing the GoF.

Respectively maximizing data–estimate correlation and GoF may produce similar results. However, in general, correlation is forgiving in terms of the estimated magnitude, which is highly affected by the skull conductivity; it was observed that the use of GoF results in a sharper global optimum, and was thus used as the optimum argument.

3.4 Source modelling

Modelling cortical activation patterns provides information on intra- and inter-areal activation. The MNS-evoked responses were localized using current dipoles and the respective source time courses were computed using minimum-norm estimation with a lead field corresponding to the sources of the three dipoles. TMS-EEG source modelling was performed using spatial priors based on the locations of the dipoles fitted to MEG data. Dipole fitting was done with the MNE-Python software using LSE and Constrained Optimization BY Linear Approximation (COBYLA) in fine-tuning the dipole parameters [60, 71].

3.4.1 Responses evoked by median nerve stimulation

While the N20m response was commonly weak in magnitude, the early temporally sharp contralateral activation patterns in SI gave rise to the ease of dipole modelling of the response. The secondary somatosensory response, P35m, arises deeper in SI and was stronger compared to N20m, and was consequently prevalent in the evoked responses. Thus, the N20m and P35m responses were easily localized using the whole MEG sensor space. However, using the N20m and P35m dipoles fitted to the whole data may result in less reliable source models due to the possible noise-induced small shifts in the dipole parameters. Hence, the N20m and P35m responses were localized using single dipoles using a subselection of axial and planar gradiometers (see Appendix B for further specifications).

In the case of localizing the bilateral P100m responses in SII, a subselection of channels (see Appendix B for further specifications) based on the anatomical location of SII was also used in dipole fitting separately for both hemispheres [72, 73, 74]. Furthermore, SI and the ipsilateral SII are anatomically adjacent and thus have two-way continuous source leakage. Hence, the dipoles reflecting activity in SII_R were fitted to the evoked responses with the prior estimated SI activity removed, if such activity was found to override activity in SII_R resulting in no plausible SII_R dipole locations. The used method is presented below.

Localizing spatiotemporally adjacent sources

1. Fit a set of dipoles \mathbf{D} (N20m and/or P35m) to the evoked response represented by sensor-level data \mathbf{m} .
2. Compute the corresponding source time courses (see Equation 14) and the respectively induced data \mathbf{m}_s at the sensor-level.
3. Calculate the difference between the original and source-induced sensor-level data to gain residual data $\mathbf{m}_r = \mathbf{m} - \mathbf{m}_s$, which is not explained by the sources of \mathbf{D} .
4. Fit a dipole to the residual data with sensor selection corresponding to SII_R and pick the most plausible dipole in terms of GoF and location.

The MNS-evoked source time courses for SI and SII were computed using MEG data with the MNE inverse operator defined in Equation 9 (where $\mathbf{R} = \mathbf{I}$ is the identity matrix

due to no prior information on the sources). The time courses $\hat{\mathbf{s}}$ were computed with the use of the localized sources, such that

$$\hat{\mathbf{s}} = \mathbf{L}_s^T (\mathbf{L}_s \mathbf{L}_s^T + \lambda^2 \mathbf{C})^{-1} \mathbf{m}, \quad (14)$$

where \mathbf{L}_s consists of the fixed orientation surface forward operators corresponding to the sources. The source orientations were fixed to the cortical mantle. The noise covariance matrix was estimated from the 300-ms pre-stimulus baseline period of the pre-processed epochs to capture both ambient and background brain noise.

The modelled sources were the SI-N20m and bilateral SII-P100m -sources found with dipole fitting. The fitted dipoles already correspond to source localization and the MNS-evoked cortical activation patterns are well known, hence, only a small regularization parameter $\lambda = 10^{-3}$ was applied. In some cases, when the GoF near the initial peaks of SI and SII was low with reliable dipole locations or clear leakage from later SI activity was observed, additional sources from SI were trialed in the source model. While the applied sources commonly increased the GoF of the model, they were rejected because their inclusion increased the spreading of the SII_R response to the respective SI time courses.

3.4.2 Responses evoked by transcranial magnetic stimulation

The MNS-evoked somatosensory responses are commonly studied using MEG and have been shown to produce consistent results in somatosensory source localization [4, 72]. As discussed in Sections 2.1.3 and 3.1.2, MEG provides a higher spatial resolution compared to EEG. Additionally, the subject-specific dipole location of N20m was used in stimulation targeting in the following TMS-experiment. Thus, for accurate comparisons between stimulus modalities, the TMS-EEG source localization was performed using prior spatial information of the dipoles fitted to MNS-MEG data.

Due to the differing stimulation modalities and stimulation site adjustments made during the measurement, the respective sources corresponding to each of the MEG-fitted dipoles can not be fully trusted as the being the same sources of TMS-evoked activity. Hence, for each source, a free-orientation dipole scan was performed for each source location estimated from MEG data. The dipoles corresponding to the highest GoF at specified time ranges were chosen as the TMS-evoked SI and SII sources. The first 10 ms were rejected from analysis due to prevalent stimulus artifacts. The stimulation was directed at SI and all subjects produced relatively high values of GoF for SI at early times, and hence, the SI dipoles were fitted to times between 10 and 25 ms. In the case of SII dipoles, a time window between 10 and 130 ms was used in dipole fitting. Larger time windows resulted in higher individual dipole GoF values, but inadequacies in the multi-dipole model.

As in the case of MEG, the sources corresponding to the fitted current dipole correspond to specific columns in the EEG lead field \mathbf{L} . While \mathbf{L} is not invertible, its pseudoinverse \mathbf{L}^\dagger can be calculated using the singular value decomposition (SVD) and used as an inverse operator. As the spatial priors gained from MEG are heavy and the TMS-evoked responses are not well known, no additional regularization was applied after the pseudoinverse is

computed, such that SI- and SII-sources are given the freedom to explain the maximum amount of the EEG data. Thus, the source time courses were computed as

$$\hat{\mathbf{s}} = \mathbf{L}_s^\dagger \mathbf{m}, \quad (15)$$

where \mathbf{L}_s holds the respective fixed orientation surface forward operators corresponding to the SI and SII current dipole sources fitted to TMS–EEG data. The approach is similar (in the sense of LSE) as in the source time course estimation from MEG data, without the inclusion of the noise covariance.

3.5 Latency detection

The N20m and the initial SI and SII TMS-evoked responses were temporally sharp. Thus, the time-lags of the responses were analyzed with the respective peak latencies. Contrarily, the bilateral MNS-evoked SII-P100m responses are temporally wider and can hold a wider peak lasting for multiple milliseconds. Thus, the actual peak of the MNS-evoked SII response is less-well defined due to the duration of activation and deviances in the source time courses caused by adjacent sources.

Many different physiological parameters ranging from individual heights to neuronal firing rates follow skewed Gaussian distributions [75]. For those MNS-evoked SII source time course peaks that were not explicit, the peak latencies were determined by computing a skewed Gaussian fit to the SII waveforms using LSE [76]. The basis of the method is to estimate the center (peak latency) T , amplitude A , skew α , and standard deviation ω of a skewed Gaussian pulse model

$$\mathbf{G}(t) = A\phi(t_s)\Phi(\alpha t_s), \quad (16)$$

where t is the time, $t_s = \frac{t-T}{\omega}$, $\phi(t) = \frac{1}{\sqrt{2\pi}} \exp(-t^2/2)$ is the standard Gaussian pulse, and $\Phi(t) = \frac{1}{2}[1 + \operatorname{erf}(\frac{t}{\sqrt{2}})]$ is its respective density function, such that

$$\{\hat{T}, \hat{A}, \hat{\alpha}, \hat{\omega}\} = \operatorname{argmin}_{\{T, A, \alpha, \omega\}} \|\hat{\mathbf{s}}_{\text{II}} - \mathbf{G}\|^2, \quad (17)$$

where $\hat{\mathbf{s}}_{\text{II}}$ is the right or left SII waveform from the multi-dipole model.

3.6 Global field amplitude

Global field amplitude (GFA) is a metric representing the overall magnitude of MEG and EEG signals in the sensor space, agnostic for the exact location of the signal source [77, 78]. Taking the unit differences in sensor-level results into account; EEG electrodes measuring electric potentials and MEG sensors (magnetometers and gradiometers) measuring magnetic fields, GFA provides a robust way for global temporal comparison of brain responses across subjects and measurement modalities. For sensors \mathbf{m} of the same type, GFA is calculated as [77]

$$\text{GFA}(t) = \sqrt{\frac{1}{N} \sum_{i=1}^N (\mathbf{m}_i(t) - \overline{\mathbf{m}}(t))^2}, \quad (18)$$

where \mathbf{m}_i is the measured data at sensor i and $\overline{\mathbf{m}}(t)$ is the mean over all N sensors at time t .

The average sensor-level results in the MNS–M/EEG protocol were calculated as the subject-wise mean over individually calculated GFA values. For summarizing topographical results for the somatosensory responses, the topographies corresponding to individual GFA peaks were aligned. In the case of the MNS-evoked bilateral SII responses, where if no clearly defined P100-corresponding GFA peaks were found, the timing of the responses were determined with visual topographical inspections of the sensor-level evoked responses. For TMS–EEG, only the temporal sensor-level GFA values were averaged due to high topographical variances.

3.7 Model validation

Source time courses describe the electrical activity of the sources over time. The estimated source time courses $\hat{\mathbf{s}}$ were used to predict the data at the sensor-level. For each time point, the source activity -induced magnetic field components and respective potential differences at the sensors were calculated as $\hat{\mathbf{m}} = \mathbf{L}_s \hat{\mathbf{s}}$, where \mathbf{L}_s consists of the columns of the lead field matrix corresponding to the sources of $\hat{\mathbf{s}}$. The constructed source models were validated by first calculating the Goodness of Fit (GoF) for all discrete time points t and then observing the GoF values corresponding to the time points near the modelled response peaks in $\hat{\mathbf{s}}$.

GoF has been a prevalent metric in validating source models via consequent source-induced topographies in M/EEG literature [79]. GoF describes the similarity between the data generated by the inversely-estimated brain activity $\hat{\mathbf{m}}$ and the measured data \mathbf{m} . A high GoF value indicates a well-fitting model while a low GoF indicates an inadequate model, which may result from the lack of modelled sources. GoF is analogous to the coefficient of determination used in linear regression and is calculated as

$$\text{GoF} \equiv 1 - \frac{\|\mathbf{m} - \hat{\mathbf{m}}\|^2}{\|\mathbf{m}\|^2}. \quad (19)$$

The dipoles fitted to TMS–EEG data were fixed to the respective locations of the dipoles fitted to MEG data, and thus, their statistical significance needed to be determined. The statistical significance of the fixed-location dipoles were determined using bootstrapping. For a time point t corresponding to the time of a fitted dipole chosen for source modelling, the respective GoF distribution was computed using a set \mathbf{D}_r of 1000 dipoles fitted to random locations in the brain at time t and calculating their values of GoF. The random locations were chosen with replacement from 8196 lead field source locations. The chosen dipoles were validated by computing their GoF percentiles in the respective GoF distributions of \mathbf{D}_r .

4 Results

4.1 Evoked responses

Evoked responses and the corresponding topographies of interest were used to validate the success of the performed measurements at the sensor level. For all subjects, GFA (see Equation 18) was calculated and averaged resulting in the measurement and sensor type specific GFA curves shown in Figure 10. All subjects elicited clear MNS-evoked activation patterns in SI visible in the full sensor space. As depicted by the standard deviations in Figure 10, the temporal consistency of the N20 responses was high while there were further deviations in the later SI responses. Furthermore, two different types of SI waveforms were observed with respectively substantially different relative magnitudes in early P35, and in later P60 and P75 SEF/P components, which are denoted by the increased waveform deviances in Figure 10. For the TMS-evoked responses, 2 prevalent peaks at approximately 15 and 50 ms were observed for all subjects; for the remainder of this thesis, the respective TMS-evoked responses will be referred to as 15_T and 50_T . Due to the differing topographies across subjects, the polarity of the responses could not be robustly defined. Similarly, as in the MNS-evoked responses, the temporal consistencies of responses are increasingly deviated with time.

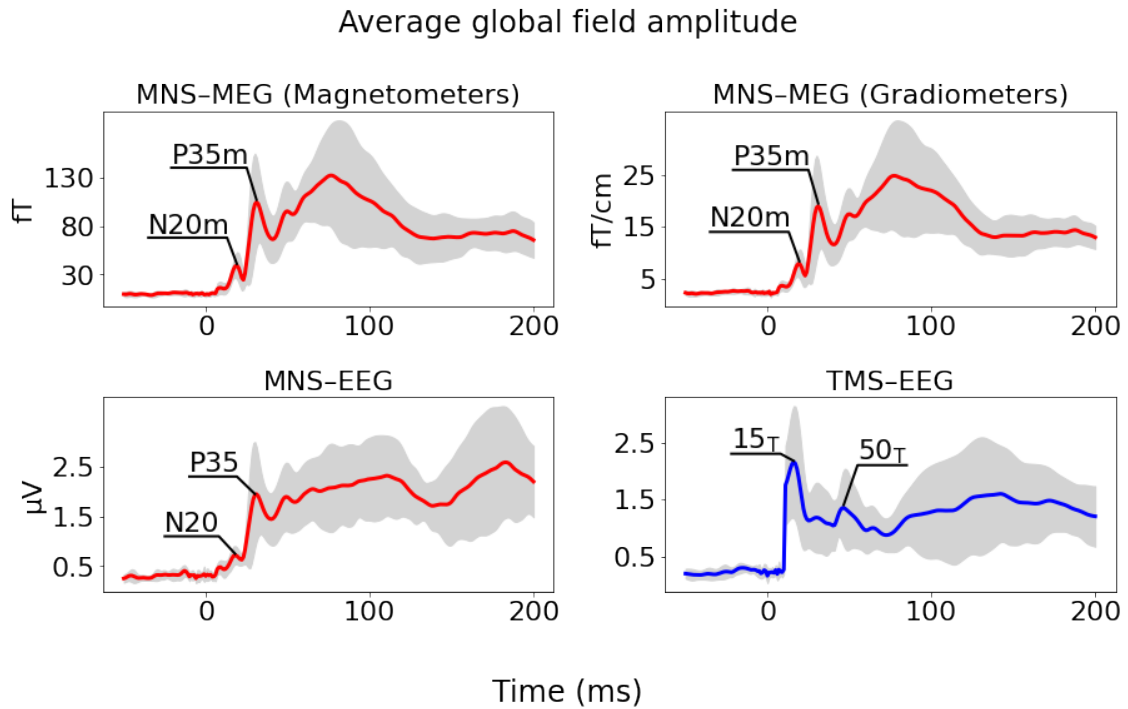


Figure 10: Average global field amplitude across measurements and sensor types. Standard deviation is denoted by the gray area. For convenience, stimulus artifact -related time windows have been replaced with noise derived from the respective baseline periods.

The topographies corresponding to the individual peaks of the MNS-evoked N20, P35, and P100 responses were averaged across sensor types and subjects (see Section 3.6), and are presented in Figure 11 below. At the topographical level, the prevalent initial N20 and P35 SEF/P components in SI were clearly visible in all subjects across all sensor types. Furthermore, even the more varying bilateral SII responses are clearly identifiable from both the MEG and EEG topographies. However, most notably in the case of P100, the average topographies are dominated by the stronger responses.

The 15_T and 50_T components were relatively consistent at the temporal scale. However, their respective spatial activation patterns differed across subjects. 15_T is depicted as both uni- and bilateral activation patterns. In turn, 50_T is more commonly represented by bilateral activation patterns at the topographical level. The topographical results suggest inter-hemispherical parallel processing between the right and left SII, with emphasis toward the right SII. However, only based on the visual topographical inspection, the exact location of a dipolar source can not be determined. Due to the large deviances across topographies, the topographical results for TMS–EEG were not averaged; for all subjects, the prevalent topographies based on GFA are presented in Appendix C.

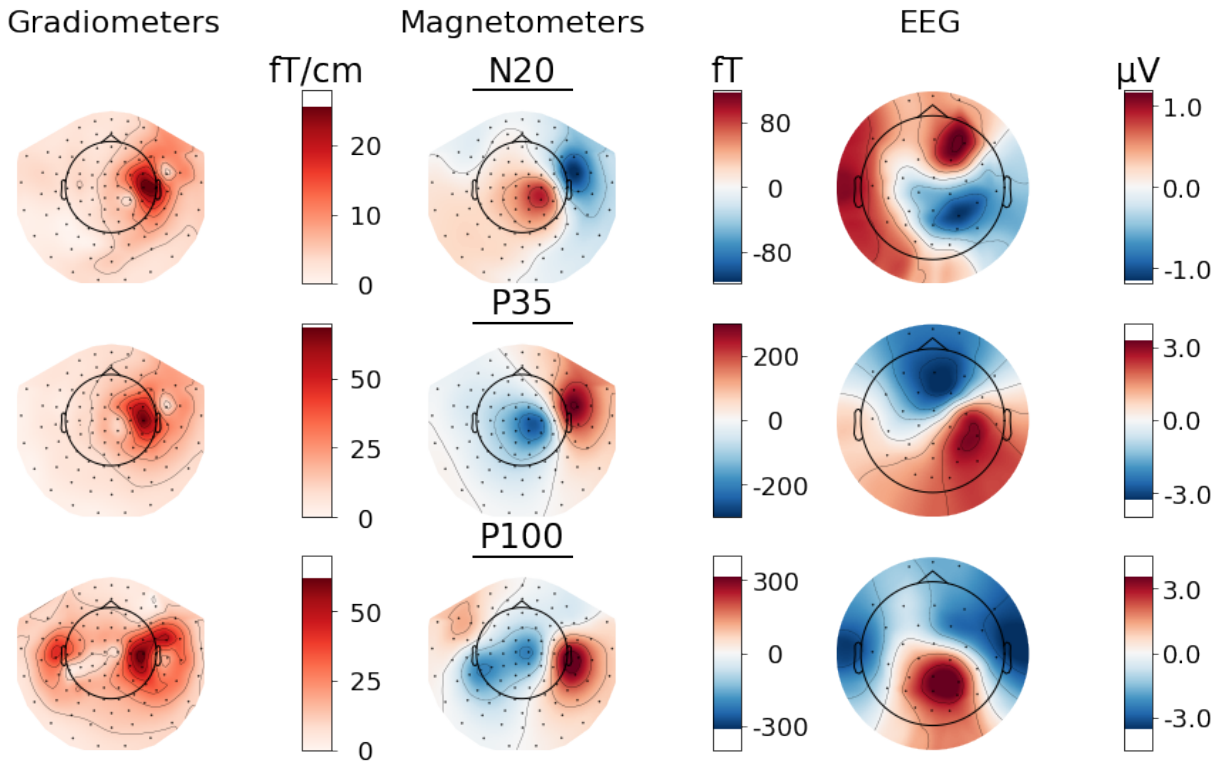


Figure 11: Averaged aligned MNS-evoked N20, P35, and P100 topographies.

4.2 Skull conductivity

Prior to TMS–EEG source modelling, three-layer BEM models with individually calibrated skull conductivity values (Section 3.3) were created for each subject using dipole modelling with the MNS-evoked P35 SEF and SEP components. The GoF was calculated for each head model with different conductivities resulting in the skull conductivity – GoF relationship -curves displayed in Figure 12 below. For each subject, the value of skull conductivity corresponding to the highest GoF was used in head modelling for TMS–EEG source modelling. A GoF maximum was found for each skull conductivity calibration procedure.

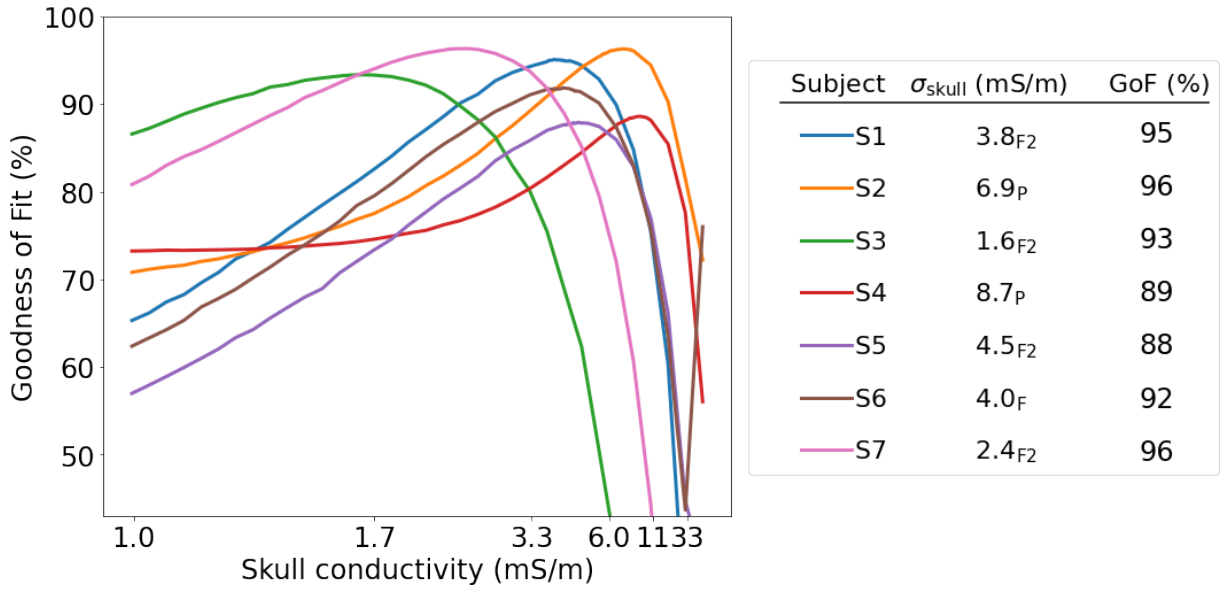


Figure 12: Skull calibration curves for all subjects. Figure legends hold the subject number, the estimated conductivity σ_{skull} , and the corresponding GoF. Indices of σ_{skull} refer to the dipole used in SEP-estimation in the calibration algorithm from Section 3.3.

The values for skull conductivity were given as scales of the conductivities of the brain and the scalp such that the last value on the x -axis (after 33 mS/m) in Figure 12 corresponds to a three-layer homogeneous 330-mS/m BEM head model. As shown by the calibration curves, the GoF substantially decreases with a high skull conductivity; except for Subject 6, where the respective GoF is increased with a homogeneous 330-mS/m BEM head model. In turn, the GoF does not decline as fast with smaller relative values of skull conductivity.

For some of the subjects, the commonly used 6-mS/m value for skull conductivity [80, 81], would have not substantially decreased the GoF; except for Subject 3, where the respective GoF declines to below 50%. For three-layer BEM head models with a skull conductivity of 6 mS/m, which in this case corresponds to a conductivity ratio of 55 between the tissues, the average GoF was $81 \pm 16\%$, which is 12% lower with higher deviation compared to the calibrated head models resulting in an average GoF of $93 \pm 3\%$. The average estimated skull conductivity was 4.6 ± 2.3 mS/m (the standard error of the mean (SEM) was 0.9 mS/m).

4.3 Somatosensory sources

The contra- and bilateral responses respectively in the right SI (N20m) and SII (P100m) evoked by electrical MNS at the left wrist were localized using dipole fitting. The same respective source locations were retrieved for TMS–EEG free-orientation source localization and consequent source time course estimation.

The spatiotemporal localization of the source corresponding to the initial N20m response could be performed for all subjects without sensor specifications. However, sensor selection was still applied for ensuring the fine tuning of the source orientations. Due to higher latencies and overlapping cortical activity and leakage from SI, there were substantial inter-subject and inter-hemispherical differences in the difficultness in the localization of the bilateral SII-P100m response. Commonly, the left hemisphere activity was easily found while localizing the activity in the right hemisphere required further steps. For all subjects, sensor selection and multiple SII-P100m dipole candidate -tuples were trialed in consequent source time course estimation. Additionally, some subjects required prior SI source time course estimation and respective component removal to enhance the prevalence of the SII_R-P100m responses (see Appendix B for specifications). The SII dipoles were picked based on their plausible location and the GoF-validated performance of the multi-dipole model. In the case of TMS–EEG, where the locations of the dipoles were pre-defined using MEG data, the dipoles were picked only based on GoF.

The relative consistencies in source estimation also show in the orientations of the fitted dipoles as shown in Table 1. As denoted by the standard deviance, the orientations of the N20m and P100m dipoles were consistent compared to the dipoles representing TMS-evoked activity – an effect further displayed in the source time courses. The average GoF values (in %) of the SI, SII_R, and SII_L dipoles fitted to TMS–EEG data were respectively 82.4 ± 6.8 , 83.7 ± 6.1 , and 78.2 ± 8.1 , respectively located at percentiles 90.7 ± 7.6 , 88.5 ± 9.7 , and 78.4 ± 11.0 , in the respective GoF distributions.

Table 1: Consistency of dipole orientations. Mean \pm SD of normalized SI and SII dipole orientations due to electric MNS at the left wrist and right-hemisphere SI TMS. R: Right hemisphere and L: Left hemisphere.

	<u>MNS–MEG</u>			<u>TMS–EEG</u>		
	x	y	z	x	y	z
	<u>Mean \pm SD</u>					
SI _R	-0.5 ± 0.1	0.7 ± 0.2	0.3 ± 0.2	-0.2 ± 0.3	0.5 ± 0.6	-0.2 ± 0.4
SII _R	-0.3 ± 0.1	0.2 ± 0.4	0.8 ± 0.2	-0.1 ± 0.3	0.0 ± 0.5	-0.6 ± 0.6
SII _L	0.2 ± 0.2	0.6 ± 0.3	0.6 ± 0.2	0.2 ± 0.5	-0.3 ± 0.5	0.0 ± 0.6

Time courses

As one would expect with the consistencies in source localization of the MNS-evoked somatosensory sources, the peaks of the SI-N20m responses were relatively consistent across all subjects while the bilateral SII-P100m response peak latencies and respective magnitudes were deviated; see Figure 13. However, for each subject, the bilateral SII peaks were still prevalent at similar times (see Appendix D). The MNS-evoked response peaks of SII_R and SII_L were wider in some subjects. Thus, respectively for Subjects 1 and 3, and Subjects 1, 2, 3, 5, and 6, the SII_R and SII_L source peak latencies were defined with the skewed Gaussian fit presented in Section 3.5. The mean difference of the times between MNS-evoked SII_R and SII_L peaks was 3.0 ms. The average peak magnitude of the MNS-evoked time courses of SII_R was higher compared to SII_L, which is in line with the sensor-level results; see the P100 topographies in Figure 11. As shown in Figure 13, while the average waveforms of TMS-evoked activity have at least one common peak, the subject-wise variability was substantially higher in all sources when compared to the MNS-evoked activity.

The values of GoF of the multi-dipole models for MNS-evoked activity, however, were not generally satisfactory. Near the respective initial peaks of SI (2-ms window), SII_R (4-ms window), and SII_L (4-ms window), the highest values of GoF (in %) were 52 ± 28 , 64 ± 18 , and 62 ± 19 , respectively. The GoF was able to be enhanced with the inclusion of additional sources from SI in the multi-dipole model. However, this resulted in the spreading of the SII_R peak to the used sources in SI, and was thus not applied. Furthermore, more visually satisfactory time courses for SII_R were found with the use of non-plausible SII_R dipole locations near SI. These were not used due to the heavy anatomical priors and to mitigate SI–SII_R leakage in the later TMS–EEG source modelling.

A substantial increase in the GoF of the multi-dipole model was commonly found near the 15_T and 50_T responses. Surprisingly, the GoF also often increased near 100 ms after the stimulus onset (100_T response). Increase in the GoF values suggests neural activity at the respective times. However, the respective peak values of GoF (in %) for the responses were 30 ± 35 , 49 ± 24 , and 44 ± 19 , which are highly deviated, and hence suggest inconsistencies in the source model and/or in the stimulation protocol, or high inter-subject differences.

As shown in Figure 13 and Appendix D, the average TMS-evoked waveforms of especially the ipsilateral SI and SII elicit similar early activation patterns. However, clear initial SI-dominant and later ongoing bilateral SII behaviour is observable. While the average SII_L waveforms also share similarities with the contralateral SI and SII waveforms, the components are more varying, on average. The information on the TMS-evoked time courses presented in Figure 13 and Table 2, are averaged results of all subjects despite the differing stimulation intensities; for subject-specific topographies and time courses, see Appendices C and D.

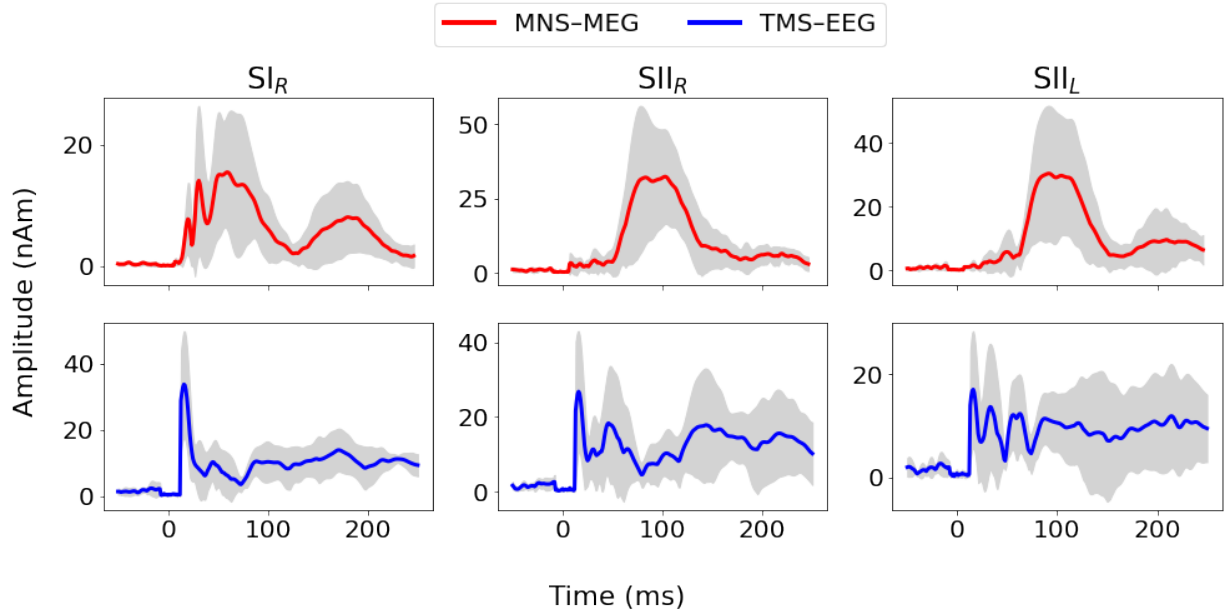


Figure 13: Average estimated time course amplitudes for SI and SII. Standard deviation is denoted by the gray area. For convenience, stimulus artifact -related time windows have been replaced with noise derived from the respective baseline periods. R: Right hemisphere and L: Left hemisphere.

Table 2: Source time course peaks. MNS-MEG: mean \pm SEM of initial SI and SII response peak magnitudes and latencies due to electric left-wrist MNS. Due to inconsistencies in the subject-wise source models, TMS-EEG: prevalent peak magnitudes and respective latencies due to right-hemisphere SI TMS in the respective average source time courses. R: Right hemisphere, L: Left hemisphere, and SEM: Standard error of the mean.

Area	MNS-MEG		TMS-EEG	
	Magnitude (nAm)	Latency (ms)	Magnitudes (nAm)	Latencies (ms)
<u>Mean \pm SEM</u>				
SI _R	8.1 \pm 2.3	19.7 \pm 0.5	(33.7, 10.3)	(16.0, 45.0)
SII _R	39.9 \pm 7.3	96.3 \pm 6.1	(26.8, 18.4, 17.9)	(16.0, 46.0, 144.0)
SII _L	35.0 \pm 7.2	99.3 \pm 4.6	(17.1, 13.6, 12.3, 11.4)	(16.0, 33.0, 63.0, 88.0)

5 Discussion

The goal of this Master's thesis was to infer the nature of connectivity between SI and SII by comparing responses in the respective areas evoked by electrical MNS at the left wrist and TMS targeted at the right-hemisphere SI, respectively measured with M/EEG and EEG.

The post-MNS-onset latencies of SII across hemispheres were relatively similar, which suggests inter-hemispherical parallel processing between the SII cortices. This is also supported by the similar latencies in the TMS-evoked waveforms. As shown in Figure 13, the MNS-evoked bilateral peaks of SII were commonly temporally wider or "w"-shaped, which suggests that SII may receive inputs from other cortical areas and from the thalamus. Although, it is possible that intra-areal SII feedback connections also play a role in the temporally wider deflections of activation, they would not explain the relatively sharper peaks of TMS-evoked activity in SII. Furthermore, there were differences in the lopsidedness of the MNS-evoked SII waveforms (see Appendix D), such that the waveforms eliciting earlier peak latencies (Subjects 3–5) were more lopsided to the left, and the other waveforms eliciting later latencies were, in comparison, more lopsided to the right. The differing lopsidedness in the responses with early vs. later deflections may respectively suggest possible inter-subject differences in the dominance of either SI-driven or thalamocortical inputs to SII. Left-hemisphere-dominant SII activity due to bilateral MNS is suggested in literature [44, 45]; given the stronger and earlier activation elicited at SII_R, it may still be that SII_L is generally dominant while the contralateral SII is dominant due to unilateral sensory stimuli.

As presented in Table 2 and Appendix D, the estimated TMS-evoked SII_R activity is stronger compared to the contralateral side, which supports SI–SII connectivity and stimulus-dependent ipsilateral SII -dominant activity. Furthermore, the less statistically significant results for the SII_L dipoles compared to the dipoles in the right hemisphere in TMS–EEG suggest stronger direct ipsilateral connectivity, or possibly no direct SI_R–SII_L connectivity. As TMS is a central stimulation method, the differences in the SII waveforms due to TMS compared to MNS suggest that SII also receives information from the peripheral nervous system bilaterally via thalamocortical pathways. It may be that the two possible signal inputs corresponding to the "w"-shaped peaks of MNS-evoked SII activity are elicited on SII_R such that the SI-driven peak precedes the peak due to inputs via thalamocortical pathways. However, the intermediate steps taken by the proposed pathway between SI–SII can not be determined based on the performed experiment. For example, the connections may also be corticothalamocortical, given the corticothalamic feedback connections from SI [58, 82]. For further assessing the nature of connectivity, additional research and dynamic causal modelling, are required.

Taking into account the hemispherical differences in the left-wrist MNS-evoked SII waveforms, SII_R may work more in conjunction with the ipsilateral SI, and that SII_L acts as an adaptive system for future processing of similar stimuli from the right side of the body. It is also possible that SII_R and SII_L are inter-hemispherically connected. However, as suggested by the deviated TMS–EEG source models and the peak topographies, the

TMS-evoked activity may arise from SI_R and SII , only from SI_R , or from nearby areas. In turn, as presented in Section 4.3, the free-orientation dipole scan resulted in relatively high values of GoF, which suggests that SI_R , SII_R , and SII_L are activated by TMS targeted at SI_R . However, due to the anatomical adjacency of the ipsilateral SI and SII and the proposed nature of bilateral SII activation, the protocol of choosing the SII_R dipoles based on GoF may have been dominated by activation in SI_R .

Limitations and improvements

Measurements

For both TMS-EEG and MNS-M/EEG measurements, the EEG preparation and defining the correct stimulation parameters, takes substantially longer compared to the actual measurement. As suggested by the noisy MNS-evoked SII waveforms in Subject 1 (see Appendix D), where only 200 median nerve stimuli were used, compared to others with 300, the inclusion of additional trials results in substantially smoother waveforms. Even though the SNR is relative to the square root of the number of trials, additional stimuli on top of the performed 300, for both measurement modalities, would be beneficial in terms of the increased SNR vs. the small additional measurement time. The increased SNR could also ease SII dipole fitting. The reduction of the intensity used in TMS for Subjects 5–7 from 120 to 90% rMT also resulted in less muscle artifacts, which should be taken into account in future measurements when stimulating the somatosensory area.

MNS and TMS are different stimulation modalities and hence evoke neuronal activity differently. MNS is a form of PNS, and can hence be assumed to activate naturally associated neurons in SI via thalamocortical pathways and in SII . However, TMS favors the activation of neurons that are closer to the scalp and specifically oriented in relation to the induced electric field. In addition, the stimulation target was adjusted for receiving a higher SNR. Hence, it is possible that those neurons in SI that are responsible for the N20 response or for the possible signal transmission between SI and SII , were not sufficiently activated.

As discussed in Section 2.3.1, contralaterally dominant bilateral activation patterns have been observed when stimulating trigeminal nerves of the face. In TMS-EEG, the coil was in constant contact with the head of the subject. Additionally, the electric field induced by the TMS pulse is felt by the subject. Thus, it is possible that the TMS-EEG data also includes activation in the left SI , which may be mixed with the supposed activity in the left SII [83]. This could explain some of the inconsistencies in the bilateral activation patterns in the TMS-EEG topographies (see Appendix C), and the differing activation patterns in SII_L compared to SII_R . All stimulations in the TMS-EEG protocol were performed with a hand-held coil, except in the case of Subject 4, where the TMS coil was mounted, and thus caused more pressure to the head of the subject. This may have constituted to the differing source-level waveforms and the least statistically significant dipoles of Subject 4 when compared to other subjects.

The TMS-EEG measurement protocol and data analysis could mitigate sensory stimuli. A slight increase of the scalp-to-coil distance would negate the effect of sensations evoked by

touch due to no physical contact between the TMS coil and the scalp. However, placing the coil to a fixed location, such that the coil is not in contact with the head of the subject, is hard in practice. In the case of the TMS-pulse-evoked sensations, little can be done as lower stimulation intensities may weaken the TMS-evoked responses relatively more compared to the weakened sensations evoked by the TMS pulse. In analysis, the possible left hemisphere SI–SII leakage could be mitigated by estimating the activity in SI_L , and then performing the dipole orientation optimization protocol to residual data with the activity from SI_L removed (similarly as with MEG data; see Section 3.4.1). The symmetry-somatotopically divided functional areas of SI are well defined, which could be used as prior information in finding the possible source location from SI_L .

Skull conductivity calibration

Skull conductivity calibration was performed individually for each subject using the secondary response in SI (P35) measured with M/EEG for enhancing the accuracy of the head model used in TMS–EEG source modelling. For each skull calibration procedure, a clear global GoF maximum was found; see Section 4.2. The GoF values at the approximated skull conductivities were higher and substantially less deviated when compared to the commonly used 6-mS/m skull conductivity value in three-layer BEM models [80, 81]. The results suggest that the individual skull conductivity calibration was successful and is a procedure that should be taken into account in simultaneous and M/EEG measurements for enhancing the efficiency of MEG and EEG source modelling.

The differing sensitivity patterns of M/EEG signals were shown especially in Subject 6, which suggests that a dynamic approach for multimodal M/EEG source localization should be taken into account. The differing dipole orientations may also be affected by the dipole location derived from MEG. For example, the SEF dipole could be used as a non-fixed spatial prior for the SEP dipole, which could be given the freedom to move in a small volume around the SEF dipole. The brain and scalp are not identical tissues, and hence, in reality, do not have the same conductivity. As the constructed method in Section 3.3 works with tissue-wise conductivity values for the brain, skull and scalp, the conductivities of the brain and scalp could also be estimated.

As shown in Figure 12, Subjects 3, 6, and 7 have slightly outlying calibration curves. These may stem from, for example, inaccurate EEG topographies or disproportionate segmentations of the skull. The cerebrospinal fluid strongly affects the volume currents, which the EEG signal is sensitive toward [84]. Thus, an additional layer corresponding to the cerebrospinal fluid could be included in the head models for acquiring more realistic results.

Median nerve stimulation -evoked responses

In practice, the protocol in fitting SII dipoles, particularly in the right hemisphere, from MEG data, was inconsistent across subjects. For finding plausible locations for the SII dipoles, different subjects required different gradiometric sensor selections, possible prior SI

source estimation, and respective component removal. While sensor selection was applied based on the anatomical location of SII and on the plausible activity seen in the sensor space, there is room left for human error, which may lead to, for example, finding no plausible sources.

A possible way for optimizing the protocol for SII dipole fitting would be to individually optimize the sensor selection by finding the best cluster of temporal gradiometers resulting in the best GoF for a dipole at a plausible location. EEG data could also be used in assessing the plausibility of the two simultaneously active dipole orientations, as the bilateral P100 SEP was also prevalent in the EEG topographies; see Figure 11. The effect of ipsilateral SI–SII leakage could also be mitigated by computing subject-specific volumetric functional regions of interest respectively based on the locations and orientations of the fitted SI and SII dipoles, such that the leakage between the regions are minimized. With the use of regional time courses, the GoF of the multi-dipole model would most likely be enhanced. For example, while the localization of the N20m dipole was consistent, its amplitude was so low that it was partially overridden by the other components, or almost completely hidden in the three-component multi-dipole model, resulting in the deviated GoF values across source models at the time of N20m. However, the inclusion of customized regions of interest could result in uncertainties in latency detection.

Transcranial magnetic stimulation -evoked responses

The TMS–EEG source time courses share common peaks, which suggests inter-areal parallel processing or inefficient independent source extraction. Based on the moderate dipole significances, it may be that different sources were also activated in the TMS protocol, and thus the dipoles fitted to pre-defined locations from MEG data may not be sufficient in TMS–EEG source estimation. The similar region-based approach discussed in the previous paragraph, as well as the inclusion of a source corresponding to SI_L , could also improve the extraction of independent sources (and improve the respective GoF values) from TMS–EEG data.

6 Conclusion

The aim of this Master's thesis was to infer the nature of connectivity between SI and SII by comparing responses in the respective areas evoked by electric MNS at the left wrist and TMS targeted at the right-hemisphere SI.

The MNS-evoked somatosensory responses were estimated in the right SI and bilaterally in SII from MEG data. The secondary somatosensory response in SI (P35) was used in estimating the skull conductivity for creating accurate individual head models for TMS–EEG source modelling. The locations of the N20m and P100m dipoles representing initial activation in SI and SII, respectively, were used as spatial priors for estimating TMS-evoked activity in the respective areas.

The skull calibration procedure increased the GoF of the P35 dipoles for all subjects. The increase in the GoF values and the orientational differences in the respective SEF and SEP components suggest that combining the information provided by the differing sensitivity patterns of MEG and EEG signals should be taken into account in future multimodal M/EEG and TMS–EEG studies. For both MNS- and TMS-evoked responses, activity in the right SI and bilateral SII activation were found. The different SII waveforms and activation latencies across hemispheres and stimulation modalities suggest that SII receives both inputs from the peripheral nervous system via thalamocortical pathways and from SI. The earlier and stronger peaks of the right-hemisphere SII due to electric MNS at the left wrist suggest that the contralateral SII is activated first, and is dominant in processing unilateral somatosensory stimuli.

References

- [1] L. R. Johnson. *Physiology of the Gastrointestinal Tract*. Elsevier, 2006.
- [2] T. I. Orenius, T. T. Raij, A. Nuortimo, P. Näätänen, J. Lipsanen, and H. Karlsson. “The interaction of emotion and pain in the insula and secondary somatosensory cortex”. In: *Neuroscience* 349 (2017), pp. 185–194.
- [3] R. Coghill. “Pain: Neuroimaging”. In: *Encyclopedia of Neuroscience*. Ed. by L. R. Squire. Oxford: Academic Press, 2009, pp. 409–414.
- [4] R. Hari and N. Forss. “Magnetoencephalography in the study of human somatosensory cortical processing”. In: *Philosophical Transactions of the Royal Society of London. Series B: Biological Sciences* 354.1387 (1999), pp. 1145–1154.
- [5] T. Yamada, R. Kayamori, J. Kimura, and D. O. Beck. “Topography of somatosensory evoked potentials after stimulation of the median nerve”. In: *Electroencephalography and Clinical Neurophysiology/Evoked Potentials Section* 59.1 (1984), pp. 29–43.
- [6] H Wikström, J Huttunen, A Korvenoja, J Virtanen, O Salonen, H Aronen, et al. “Effects of interstimulus interval on somatosensory evoked magnetic fields (SEFs): A hypothesis concerning SEF generation at the primary sensorimotor cortex”. In: *Electroencephalography and Clinical Neurophysiology/Evoked Potentials Section* 100.6 (1996), pp. 479–487.
- [7] C. Daubin, D. Guillotin, O. Etard, C. Gaillard, D. du Cheyron, M. Ramakers, et al. “A clinical and EEG scoring system that predicts early cortical response (N20) to somatosensory evoked potentials and outcome after cardiac arrest”. In: *BMC Cardiovascular Disorders* 8.1 (2008), pp. 1–9.
- [8] N. Forss, M. Hietanen, O. Salonen, and R. Hari. “Modified activation of somatosensory cortical network in patients with right-hemisphere stroke”. In: *Brain : A Journal of Neurology* 122 (Pt 10) (Nov. 1999), pp. 1889–99.
- [9] B. Taskin, G. J. Jungehulsing, J. Ruben, P. Brunecker, T. Krause, F. Blankenburg, et al. “Preserved responsiveness of secondary somatosensory cortex in patients with thalamic stroke”. In: *Cerebral Cortex* 16.10 (Dec. 2005), pp. 1431–1439.
- [10] A. T. Barker, R. Jalinous, and I. L. Freeston. “Non-invasive magnetic stimulation of human motor cortex”. In: *The Lancet* 325.8437 (1985), pp. 1106–1107.
- [11] R. J. Ilmoniemi, J Ruohonen, and J. Karhu. “Transcranial magnetic stimulation—A new tool for functional imaging”. In: *Critical Reviews in Biomedical Engineering* 27 (1999), pp. 241–284.
- [12] R. J. Ilmoniemi and J. Sarvas. *Brain signals: Physics and Mathematics of MEG and EEG*. Mit Press, 2019.
- [13] M. Catani. “Neuroanatomical bases of human behavior”. In: *Encyclopedia of Behavioral Neuroscience, 2nd Edition (Second Edition)*. Ed. by S. Della Sala. Second Edition. Oxford: Elsevier, 2022, pp. 60–64.

- [14] S. Murakami and Y. Okada. “Contributions of principal neocortical neurons to magnetoencephalography and electroencephalography signals”. In: *The Journal of Physiology* 575.3 (2006), pp. 925–936.
- [15] H. Kaltiainen, M. Liljeström, L. Helle, A. Salo, M. Hietanen, H. Renvall, et al. “Mild traumatic brain injury affects cognitive processing and modifies oscillatory brain activity during attentional tasks”. In: *Journal of Neurotrauma* 36.14 (2019), pp. 2222–2232.
- [16] C. Fanciullacci, A. Panarese, V. Spina, M. Lassi, A. Mazzoni, F. Artoni, et al. “Connectivity measures differentiate cortical and subcortical sub-acute ischemic stroke patients”. In: *Frontiers in Human Neuroscience* 15 (2021), p. 368.
- [17] B. Lanfer, M. Scherg, M. Dannhauer, T. R. Knösche, M. Burger, and C. H. Wolters. “Influences of skull segmentation inaccuracies on EEG source analysis”. In: *NeuroImage* 62.1 (2012), pp. 418–431.
- [18] M. Hämäläinen, R. Hari, R. J. Ilmoniemi, J. Knuutila, and O. V. Lounasmaa. “Magnetoencephalography—theory, instrumentation, and applications to noninvasive studies of the working human brain”. In: *Reviews of Modern Physics* 65.2 (1993), p. 413.
- [19] M. Antonakakis, S. Schrader, Ü. Aydin, A. Khan, J. Gross, M. Zervakis, et al. “Inter-subject variability of skull conductivity and thickness in calibrated realistic head models”. In: *NeuroImage* 223 (2020), p. 117353.
- [20] Ü. Aydin, J. Vorwerk, P. Küpper, M. Heers, H. Kugel, A. Galka, et al. “Combining EEG and MEG for the reconstruction of epileptic activity using a calibrated realistic volume conductor model”. In: *Plos One* 9.3 (2014), e93154.
- [21] O. Hauk, D. G. Wakeman, and R. Henson. “Comparison of noise-normalized minimum norm estimates for MEG analysis using multiple resolution metrics”. In: *NeuroImage* 54.3 (2011), pp. 1966–1974.
- [22] M. Hämäläinen and R. Ilmoniemi. “Interpreting measured magnetic fields of the brain: Estimates of current distributions”. In: *University of Helsinki, Finland, Technical Report TKK-F-A559* (1984).
- [23] R. A. Willoughby. “Solutions of ill-posed problems (AN Tikhonov and VY Arsenin)”. In: *SIAM Review* 21.2 (1979), p. 266.
- [24] A.-S. Hincapié, J. Kujala, J. Mattout, S. Daligault, C. Delpuech, D. Mery, et al. “MEG connectivity and power detections with minimum norm estimates require different regularization parameters”. In: *Computational Intelligence and Neuroscience* 2016 (2016).
- [25] F.-H. Lin, T. Witzel, M. S. Hämäläinen, A. M. Dale, J. W. Belliveau, and S. M. Stuffelbeem. “Spectral spatiotemporal imaging of cortical oscillations and interactions in the human brain”. In: *NeuroImage* 23.2 (2004), pp. 582–595.

- [26] A. M. Dale, A. K. Liu, B. R. Fischl, R. L. Buckner, J. W. Belliveau, J. D. Lewine, et al. “Dynamic statistical parametric mapping: Combining fMRI and MEG for high-resolution imaging of cortical activity”. In: *Neuron* 26.1 (2000), pp. 55–67.
- [27] A. S. Aberra, B. Wang, W. M. Grill, and A. V. Peterchev. “Simulation of transcranial magnetic stimulation in head model with morphologically-realistic cortical neurons”. In: *Brain Stimulation* 13.1 (2020), pp. 175–189.
- [28] J.-P. Lefaucheur, A. Aleman, C. Baeken, D. H. Benninger, J. Brunelin, V. Di Lazzaro, et al. “Evidence-based guidelines on the therapeutic use of repetitive transcranial magnetic stimulation (rTMS): An update (2014–2018)”. In: *Clinical Neurophysiology* 131.2 (2020), pp. 474–528.
- [29] L. M. Koponen, J. O. Nieminen, and R. J. Ilmoniemi. “Multi-locus transcranial magnetic stimulation—theory and implementation”. In: *Brain Stimulation* 11.4 (2018), pp. 849–855.
- [30] H. Hannula and R. Ilmoniemi. “Basic principles of navigated TMS”. English. In: *Navigated Transcranial Magnetic Stimulation in Neurosurgery*. Ed. by S. Krieg. Switzerland: Springer, 2017, pp. 3–29. ISBN: 978-3-319-54917-0.
- [31] R. J. Ilmoniemi, J. Virtanen, J. Ruohonen, J. Karhu, H. J. Aronen, R. Näätänen, et al. “Neuronal responses to magnetic stimulation reveal cortical reactivity and connectivity”. In: *Neuroreport* 8.16 (1997), pp. 3537–3540.
- [32] R. Treede and A. Apkarian. “5.45 - Nociceptive processing in the cerebral cortex”. In: *The Senses: A Comprehensive Reference*. New York: Academic Press, 2008, pp. 669–697.
- [33] L. M. Biga, S. Dawson, A. Harwell, R. Hopkins, J. Kaufmann, M. LeMaster, et al. *Anatomy & Physiology*. OpenStax/Oregon State University, 2020.
- [34] M. Bennett and P. Jannetta. “Trigeminal evoked potentials in humans”. In: *Electroencephalography and Clinical Neurophysiology* 48.5 (1980), pp. 517–526.
- [35] I. Hashimoto. “Trigeminal evoked potentials following brief air puff: Enhanced signal-to-noise ratio”. In: *Annals of Neurology* 23.4 (1988), pp. 332–338.
- [36] J. Feher. “4.3 - Cutaneous sensory systems”. In: *Quantitative Human Physiology (Second Edition)*. Ed. by J. Feher. Second Edition. Boston: Academic Press, 2012, pp. 389–399.
- [37] M. J. Brown, A. Weissbach, M. G. Pauly, M. Vesia, C. Gunraj, J. Baarbé, et al. “Somatosensory-motor cortex interactions measured using dual-site transcranial magnetic stimulation”. In: *Brain Stimulation* 12.5 (2019), pp. 1229–1243.
- [38] M. Borich, S. Brodie, W. Gray, S. Ionta, and L. Boyd. “Understanding the role of the primary somatosensory cortex: Opportunities for rehabilitation”. In: *Neuropsychologia* 79 (2015), pp. 246–255.

- [39] J. Driver and T. Noesselt. “Multisensory interplay reveals crossmodal influences on ‘sensory-specific’ brain regions, neural responses, and judgments”. In: *Neuron* 57.1 (2008), pp. 11–23.
- [40] L. Lauronen, E. Heikkilä, T. Autti, K. Sainio, J. Huttunen, H. J. Aronen, et al. “Somatosensory evoked magnetic fields from primary sensorimotor cortex in juvenile neuronal ceroid lipofuscinosis”. In: *Journal of Child Neurology* 12.6 (1997), pp. 355–360.
- [41] R. Kakigi. “Somatosensory evoked magnetic fields following median nerve stimulation”. In: *Neuroscience Research* 20.2 (1994), pp. 165–174.
- [42] K. Zilles and N. Palomero-Gallagher. “4.14 - The architecture of somatosensory cortex”. In: *The Senses: A Comprehensive Reference (Second Edition)*. Ed. by B. Fritzsche. Second Edition. Oxford: Elsevier, 2020, pp. 225–260.
- [43] E. Disbrow, T. Roberts, D. Poeppel, and L. Krubitzer. “Evidence for interhemispheric processing of inputs from the hands in human S2 and PV”. In: *Journal of Neurophysiology* 85 (June 2001), pp. 2236–44.
- [44] C. Simoes, F. Alary, N. Forss, and R. Hari. “Left-hemisphere-dominant SII activation after bilateral median nerve stimulation”. In: *NeuroImage* 15.3 (2002), pp. 686–690.
- [45] N. Forss, R. Hari, R. Salmelin, A. Ahonen, M. Hämäläinen, M. Kajola, et al. “Activation of the human posterior parietal cortex by median nerve stimulation”. In: *Experimental Brain Research* 99.2 (1994), pp. 309–315.
- [46] C. J. Cascio. “Somatosensory processing in neurodevelopmental disorders”. In: *Journal of Neurodevelopmental Disorders* 2.2 (2010), pp. 62–69.
- [47] R. J. Maldonado and O. De Jesus. *Hyperesthesia*. StatPearls Publishing, Treasure Island (FL), 2022. URL: <http://europepmc.org/books/NBK563125>.
- [48] C. L. Reed and M. Ziat. “Haptic perception: From the skin to the brain”. In: *Reference Module in Neuroscience and Biobehavioral Psychology*. Elsevier, 2018.
- [49] D. Bouhassira, M. Lantéri-Minet, N. Attal, B. Laurent, and C. Touboul. “Prevalence of chronic pain with neuropathic characteristics in the general population”. In: *Pain* 136.3 (2008), pp. 380–387.
- [50] N. Torrance, B. H. Smith, M. I. Bennett, and A. J. Lee. “The epidemiology of chronic pain of predominantly neuropathic origin. Results from a general population survey”. In: *The Journal of Pain* 7.4 (2006), pp. 281–289.
- [51] J. Sheng, S. Liu, Y. Wang, R. Cui, and X. Zhang. “The link between depression and chronic pain: neural mechanisms in the brain.” In: *Neural Plasticity* (2017).
- [52] M. V. Seeman. “Psychopathology in women and men: Focus on female hormones”. In: *American Journal of Psychiatry* 154.12 (1997), pp. 1641–1647.
- [53] M. L. Phillips, W. C. Drevets, S. L. Rauch, and R. Lane. “Neurobiology of emotion perception II: Implications for major psychiatric disorders”. In: *Biological Psychiatry* 54.5 (2003), pp. 515–528.

- [54] R. Dolan. “Emotion, cognition, and behavior”. In: *Science (New York, N.Y.)* 298 (Dec. 2002), pp. 1191–4.
- [55] E. Kropf, S. K. Syan, L. Minuzzi, and B. N. Frey. “From anatomy to function: The role of the somatosensory cortex in emotional regulation”. In: *Brazilian Journal of Psychiatry* 41 (2018), pp. 261–269.
- [56] D. D. Price. “Psychological and neural mechanisms of the affective dimension of pain”. In: *Science* 288.5472 (2000), pp. 1769–1772.
- [57] D. A. Fishbain, R. Cutler, H. L. Rosomoff, and R. S. Rosomoff. “Chronic pain-associated depression: Antecedent or consequence of chronic pain? A review”. In: *The Clinical Journal of Pain* 13.2 (1997), pp. 116–137.
- [58] Y. Song, Q. Su, Q. Yang, R. Zhao, G. Yin, W. Qin, et al. “Feedforward and feedback pathways of nociceptive and tactile processing in human somatosensory system: A study of dynamic causal modeling of fMRI data”. In: *NeuroImage* 234 (2021), p. 117957.
- [59] G. H. Glover. “Overview of functional magnetic resonance imaging”. In: *Neurosurgery Clinics* 22.2 (2011), pp. 133–139.
- [60] A. Gramfort, M. Luessi, E. Larson, D. A. Engemann, D. Strohmeier, C. Brodbeck, et al. “MEG and EEG data analysis with MNE-Python”. In: *Frontiers in Neuroscience* 7.267 (2013), pp. 1–13.
- [61] A. Delorme and S. Makeig. “EEGLAB: an open source toolbox for analysis of single-trial EEG dynamics including independent component analysis”. In: *Journal of Neuroscience Methods* 134.1 (2004), pp. 9–21.
- [62] T. P. Mutanen, M. Biabani, J. Sarvas, R. J. Ilmoniemi, and N. C. Rogasch. “Source-based artifact-rejection techniques available in TESA, an open-source TMS–EEG toolbox”. In: *Brain Stimulation: Basic, Translational, and Clinical Research in Neuromodulation* 13.5 (2020), pp. 1349–1351.
- [63] N. C. Rogasch, C. Sullivan, R. H. Thomson, N. S. Rose, N. W. Bailey, P. B. Fitzgerald, et al. “Analysing concurrent transcranial magnetic stimulation and electroencephalographic data: A review and introduction to the open-source TESA software”. In: *NeuroImage* 147 (2017), pp. 934–951.
- [64] P. Comon. “Independent component analysis, a new concept?” In: *Signal Processing* 36.3 (1994), pp. 287–314.
- [65] T. P. Mutanen, J. Metsomaa, S. Liljander, and R. J. Ilmoniemi. “Automatic and robust noise suppression in EEG and MEG: The SOUND algorithm”. In: *NeuroImage* 166 (2018), pp. 135–151.
- [66] T. P. Mutanen, M. Kukkonen, J. O. Nieminen, M. Stenroos, J. Sarvas, and R. J. Ilmoniemi. “Recovering TMS-evoked EEG responses masked by muscle artifacts”. In: *NeuroImage* 139 (2016), pp. 157–166.

- [67] M. Reuter, N. J. Schmansky, H. D. Rosas, and B. Fischl. “Within-subject template estimation for unbiased longitudinal image analysis”. In: *NeuroImage* 61.4 (2012), pp. 1402–1418.
- [68] F. Ségonne, A. M. Dale, E. Busa, M. Glessner, D. Salat, H. K. Hahn, et al. “A hybrid approach to the skull stripping problem in MRI”. In: *NeuroImage* 22.3 (2004), pp. 1060–1075.
- [69] H. McCann, G. Pisano, and L. Beltrachini. “Variation in reported human head tissue electrical conductivity values”. In: *Brain Topography* 32.5 (2019), pp. 825–858.
- [70] J. Vorwerk, Ü. Aydin, C. H. Wolters, and C. R. Butson. “Influence of head tissue conductivity uncertainties on EEG dipole reconstruction”. In: *Frontiers in Neuroscience* 13 (2019), p. 531.
- [71] M. J. Powell. “A view of algorithms for optimization without derivatives”. In: *Mathematics Today-Bulletin of the Institute of Mathematics and its Applications* 43.5 (2007), pp. 170–174.
- [72] C. Simões, O. Jensen, L. Parkkonen, and R. Hari. “Phase locking between human primary and secondary somatosensory cortices”. In: *Proceedings of the National Academy of Sciences* 100.5 (2003), pp. 2691–2694.
- [73] R. J. Thoma, F. M. Hanlon, M. Huang, G. A. Miller, S. N. Moses, M. P. Weisend, et al. “Impaired secondary somatosensory gating in patients with schizophrenia”. In: *Psychiatry Research* 151.3 (2007), pp. 189–199.
- [74] M. Kallio. “Activity in somatosensory cortices during stroke recovery”. English. Master’s thesis. Aalto University. School of Science, 2018, pp. 63+2. URL: <http://urn.fi/URN:NBN:fi:aalto-201806293925>.
- [75] G. Buzsáki and K. Mizuseki. “The log-dynamic brain: How skewed distributions affect network operations”. In: *Nature Reviews Neuroscience* 15.4 (2014), pp. 264–278.
- [76] P. Virtanen, R. Gommers, T. E. Oliphant, M. Haberland, T. Reddy, D. Cournapeau, et al. “SciPy 1.0: Fundamental algorithms for scientific computing in Python”. In: *Nature Methods* 17 (2020), pp. 261–272.
- [77] D. Lehmann and W. Skrandies. “Reference-free identification of components of checkerboard-evoked multichannel potential fields”. In: *Electroencephalography and Clinical Neurophysiology* 48.6 (1980), pp. 609–621.
- [78] S. Esser, R. Huber, M. Massimini, M. Peterson, F. Ferrarelli, and G. Tononi. “A direct demonstration of cortical LTP in humans: a combined TMS/EEG study”. In: *Brain Research Bulletin* 69.1 (2006), pp. 86–94.
- [79] E. Kaukoranta, M. Hämäläinen, J. Sarvas, and R. Hari. “Mixed and sensory nerve stimulations activate different cytoarchitectonic areas in the human primary somatosensory cortex SI”. In: *Experimental Brain Research* 63.1 (1986), pp. 60–66.
- [80] Y. Petrov and S. Sridhar. “Electric field encephalography as a tool for functional brain research: a modeling study”. In: *Plos One* 8.7 (2013), e67692.

- [81] J. G. Samuelsson, N. Peled, F. Mamashli, J. Ahveninen, and M. S. Hämäläinen. “Spatial fidelity of MEG/EEG source estimates: A general evaluation approach”. In: *NeuroImage* 224 (2021), p. 117430.
- [82] A. Groh and R. Mease. “Corticothalamic pathways in the somatosensory system”. In: *The Thalamus*. Ed. by M. M. Halassa. Cambridge University Press, 2022, 221–236.
- [83] V. Conde, L. Tomasevic, I. Akopian, K. Stanek, G. B. Saturnino, A. Thielscher, et al. “The non-transcranial TMS-evoked potential is an inherent source of ambiguity in TMS-EEG studies”. In: *NeuroImage* 185 (2019), pp. 300–312.
- [84] M. Stenroos and A. Nummenmaa. “Incorporating and compensating cerebrospinal fluid in surface-based forward models of magneto-and electroencephalography”. In: *Plos One* 11.7 (2016), e0159595.

Appendix

A Measurement information

Table A1: Measurement and stimulation parameters. Stimulation counts and measurement durations are approximated.

Parameter	MNS–M/EEG	TMS–EEG
<u>Measurement</u>		
System	MEGIN TRIUX TM neo	Bittium NeurOne TM
Measurement channels	102 magnetometers + 206 gradiometers + 32 EEG	62 EEG
Additional channels	1 bipolar EOG	-
Sampling rate (Hz)	1000	5000
Duration	3x5 min	3x3 min
<u>Stimulation</u>		
Type	Electric MNS at the left wrist	TMS to the right SI
Intensity	150% rMT	120 or 90% rMT
ISI	3 s	2.0–2.3 s
Stimuli/block	100	100
Total stimuli	300	300

For the pilot measurements (Subject 1), only the protocol in MNS–M/EEG differed from those under the ethical permit: the measurement consisted of 200 stimuli in 1 block. The ground electrode was attached to the head rather than to the left arm.

For Subject 6, the MNS–M/EEG measurements included one additional block due to the stimulator shifting away from the stimulation spot during the first block. The data from the first block was not included in the analysis.

For Subject 5, in TMS–EEG, using the 120% rMT stimulation intensity did not result in as visually clear responses. Hence, the stimulation intensity was adjusted to 90% rMT (initially as a trial), which evoked TEPs and caused a smaller magnitude in muscle artifacts. The stimulation intensity was thus also adjusted to 90% rMT for the later TMS–EEG measurements (Subjects 6 and 7).

B Sensor selection

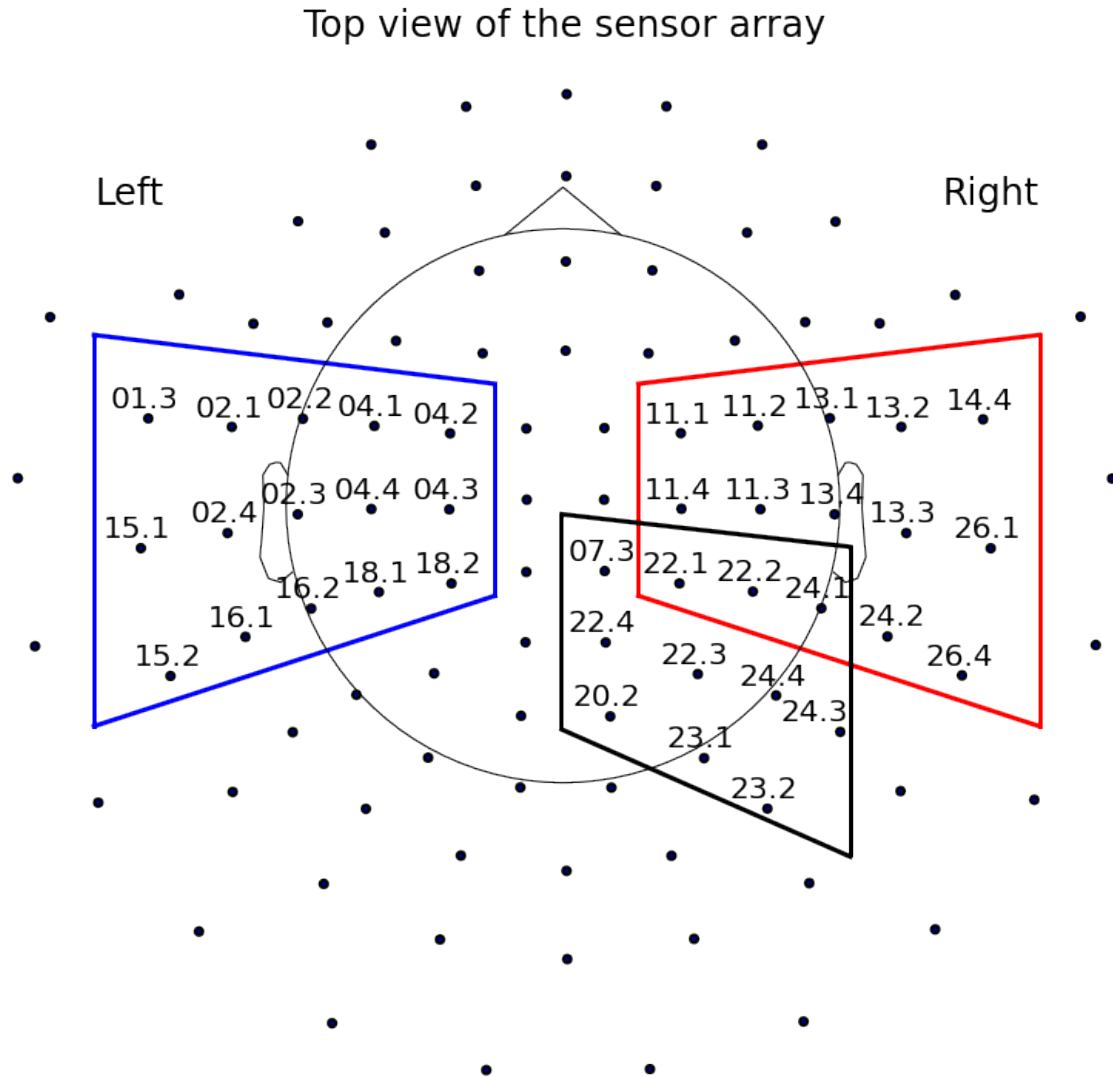


Figure B1: General MEG gradiometric sensor selections. The sensors are used in dipole fitting to the responses in SI (N20m and P35m, using both planar and axial gradiometers) and SII (P100m, using planar gradiometers). Outlines depict the general area of sensor selection: Black: Right SI, Red: Right SII, and Blue: Left SII.

Specifications

This section presents further specifications for the applied dipole fitting protocols for the MNS–MEG multi-dipole model and for the P35m dipole in skull conductivity calibration. If no specifications for a specific dipole is presented, then the dipole was fitted using the respective channels presented in Figure B1 above. Each dipole fitting protocol was attempted without specifications and was adjusted if no plausible dipoles were found.

Subject 1: Both planar and axial gradiometers (not including sensors 04.2, 04.3, and 18.2) were used for SII_L dipole fitting. Planar gradiometers from sensors 13.4, 24.1, 24.4, 22.2, 11.3, 11.2, 13.1, and 13.2, were used in SII_R dipole fitting.

Subject 2: Sensors 04.2, 04.3, 18.2, 11.1, 11.4, and 22.1 were not used in respective SII_L dipole fitting and the contralateral SII_R dipole was fitted with a free orientation using planar gradiometers in sensors 13.4, 24.1, 24.4, 24.1, 22.2, and 11.3 to the respective contralateral location of the SII_L dipole.

Subject 3: The SII_R dipole was fitted using planar gradiometers in the union of the representative SII_R and SI sensor groups. The SII_R dipole was also fitted using the residual fitting technique presented in Section 3.4.1.

Subject 4: None.

Subject 5: The SII_R dipole was fitted using the residual fitting technique presented in Section 3.4.1.

Subject 6: No sensor selection was applied in N20m or P35m dipole fitting. The overlapping representative SI channels were not used in SII_R dipole fitting.

Subject 7: No sensor selection was applied in N20m or P35m dipole fitting. The overlapping representative SI channels were not used in SII_R dipole fitting. The SII_R dipole was also fitted using the residual fitting technique presented in Section 3.4.1. Sensors 04.2, 04.3, and 18.2 were not used in SII_L dipole fitting.

C TEP peak topographies

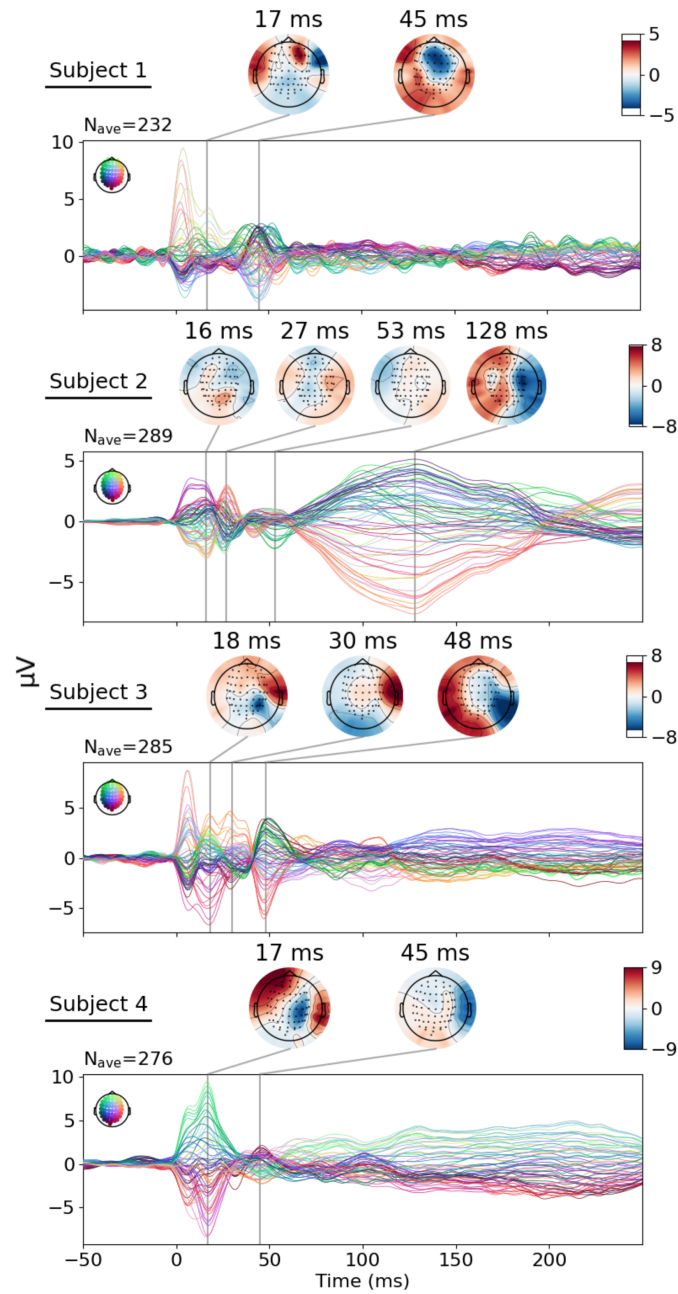


Figure C1: Sensor-level TEPs for Subjects 1–4. The stimulation intensity was 120% rMT. Stimulation artifacts are prevalent during the first ~ 10 ms post-stimulation.

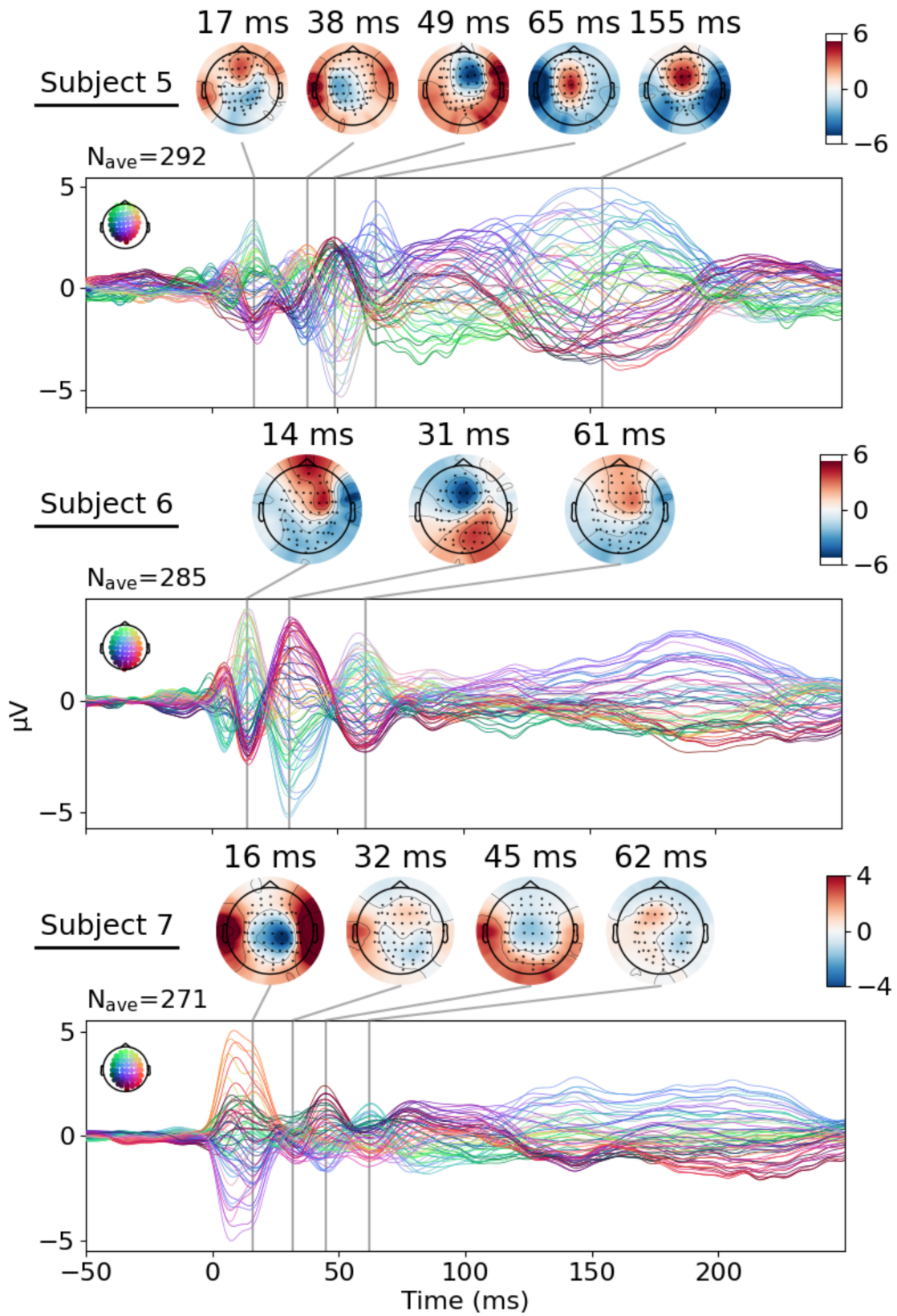


Figure C2: Sensor-level TEPs for Subjects 5–7. The stimulation intensity was 90% rMT. Stimulation artifacts are prevalent during the first ~ 10 ms post-stimulation.

D Somatosensory time courses

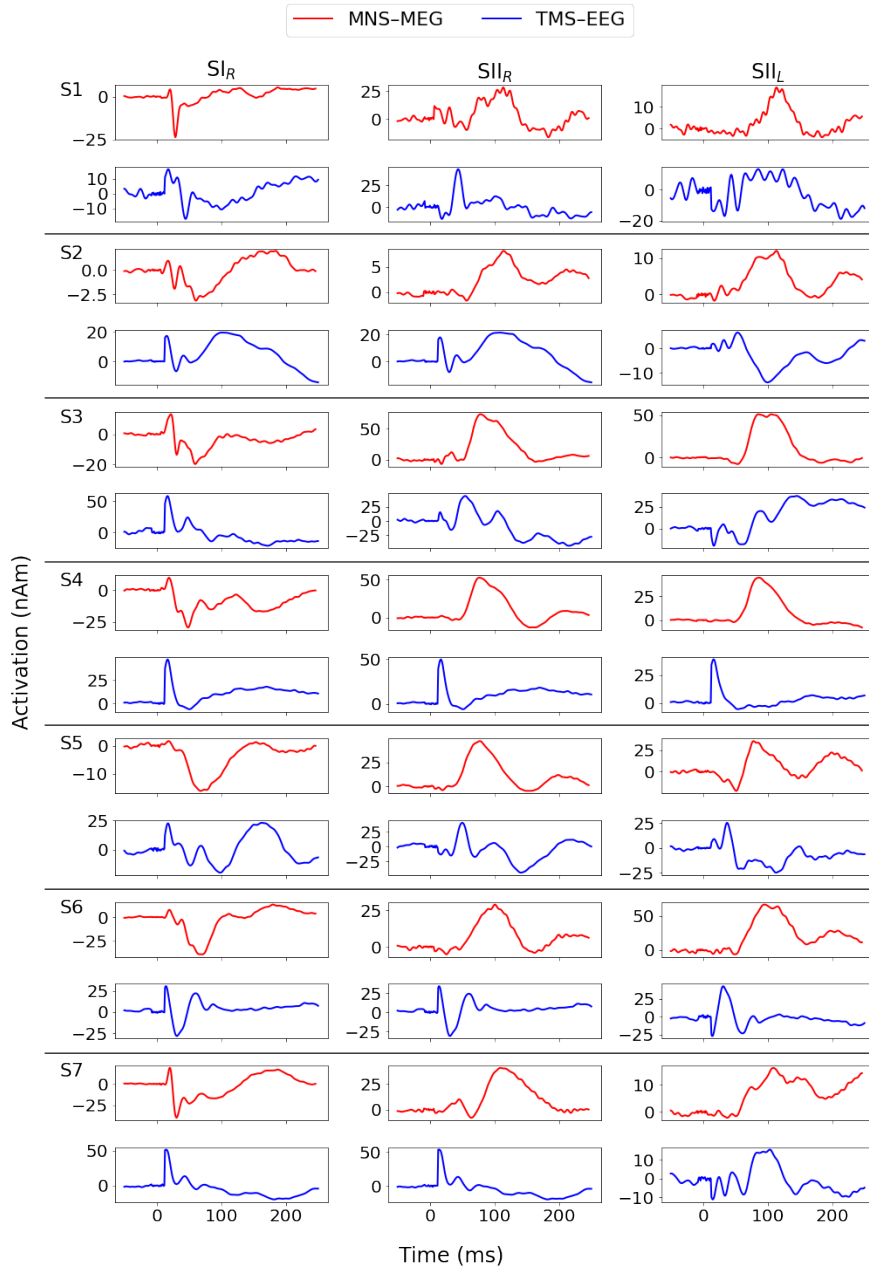


Figure D1: Estimated time courses in SI and SII for all subjects. For convenience, stimulus artifact -related time windows have been replaced with noise derived from the respective baseline periods.